**Astronomy & Astrophysics**

# Deriving metallicities from calcium triplet spectroscopy in combination with near-infrared photometry[*],[**],[***]

F. Mauro[1], C. Moni Bidin[1,2], D. Geisler[1], I. Saviane[3], G. S. Da Costa[4], A. C. Gormaz-Matamala[1], S. Vasquez[3,5], A.-N. Chené[1,6,7], R. Cohen[1], and B. Dias[3,8]

[1] Departamento de Astronomía, Universidad de Concepción, Casilla 160-C, Concepción, Chile
e-mail: skz5k2@gmail.com
[2] Instituto de Astronomía, Universidad Católica del Norte, Av. Angamos 0610, Casilla 1280, Antofagasta, Chile
[3] European Southern Observatory, Ave. Alonso de Cordova 3107, Casilla 19, 19001 Santiago, Chile
[4] Research School of Astronomy & Astrophyiscs, Australian National University, Canberra ACT 0200, Australia
[5] Instituto de Astrofísica, Facultad de Fisíca, Pontificia Universidad Católica de Chile, Av. Vicuña MacKenna 4860, Santiago, Chile
[6] Gemini Observatory, Hawaii, USA
[7] Departamento de Fisíca y Astronomía, Universidad de Valparaíso, Av. Gran Bretaña 1111, Casilla 5030, Playa Ancha, Chile
[8] Instituto de Astronomia, Geofísica e Ciências Atmosféricas, Universidade de São Paulo, rua do Matão 1226, Cidade Universitária, 05508-900 São Paulo, Brazil

## ABSTRACT

*Context.* When they are established with sufficient precision, the ages, metallicities and kinematics of Galactic globular clusters (GGCs) can shed much light on the dynamical and chemical evolution of the Galactic halo and bulge. While the most fundamental way of determining GC abundances is by means of high-resolution spectroscopy, in practice this method is limited to only the brighter stars in the nearest and less reddened objects. This restriction has, over the years, led to the development of a large number of techniques that measure the overall abundance indirectly from parameters that correlate with overall metallicity. One of the most efficient methods is measuring the equivalent width (EW) of the calcium II triplet (CaT) at $\lambda \approx 8500$ Å in red giants, which are corrected for the luminosity and temperature effects using the $V$ magnitude differences from the horizontal branch (HB).
*Aims.* We establish a similar method in the near-infrared (NIR), by combining the power of the differential magnitudes technique with the advantages of NIR photometry to minimize differential reddening effects.
*Methods.* We used the $K_s$ magnitude difference between the star and the reddest part of the HB (RHB) or of the red clump (RC) to generate reduced equivalent widths (rEW) from previously presented datasets. Then we calibrated these rEW against three previously reported different metallicity scales; one of which we corrected using high-resolution spectroscopic metallicities.
*Results.* We calculated the calibration relations for the two datasets and the three metallicity scales and found that they are approximately equivalent, with almost negligible differences. We compared our NIR calibrations with the corresponding optical ones, and found them to be equivalent, which shows that the luminosity-corrected rEW using the $K_s$ magnitude is compatible with the one obtained from the $V$ magnitude. We then used the metallicities obtained from the calibration to investigate the internal metallicity distributions of the GCs.
*Conclusions.* We have established that the ([Fe/H]:rEW) relation is independent of the magnitude used for the luminosity correction and find that the calibration relations change only slightly for different metallicity scales. The CaT technique using NIR photometry is thus a powerful tool to derive metallicities. In particular, it can be used to study the internal metallicity spread of a GC. We confirm the presence of at least two metallicity populations in NGC 6656 and find that several other GCs present peculiar metallicity distributions.

**Key words.** stars: abundances – globular clusters: general – stars: kinematics and dynamics

## 1. Introduction

Stellar population studies are among our most powerful tools for investigating a wide variety of fundamental problems in stellar and galactic astrophysics. In particular, globular clusters (GCs) are perfect laboratories in this regard. They are testbeds for the understanding not only of stellar evolution and

dynamics, but also of the formation of stellar exotica and the processes leading to the disruption of massive stellar systems. GCs are cornerstones of the distance scale and serve as dynamical probes of a galaxy's complex kinematics and interaction history. They are unegualed as tracers of the structure, formation and chemical evolution of a galaxy and its distinct components. Galactic GCs (GGCs) represent one of the fundamental systems that allow a reconstruction of the early evolution of the Milky Way: the knowledge of their ages, metallicities and kinematics has shed much light on the dynamical and chemical evolution of the Galactic halo and bulge (Zinn 1985; Minniti 1995; Ferraro et al. 2009).

While the most fundamental way of determining GC abundances is through high-resolution (HR) spectroscopy, in practice

---

this method is limited to only the brighter stars in the nearest GCs. This restriction has led over the years to the development of a large number of techniques aimed at indirectly measuring the overall metal abundance by using parameters such as the line strength, blanketing, or giant branch effective temperature, all of which correlate with the overall metallicity. Even if these indices strictly speaking only provide criteria for ranking clusters by abundance, actual metallicities can be determined with appropriate calibration.

One of the most efficient methods is measuring the equivalent width (EW) of the calcium II triplet (CaT) at $\lambda \approx 8500$ Å in red giants (Olszewski et al. 1991; Armandroff & Da Costa 1991). This technique has many advantages. It is one of the most efficient ways to build up a large sample of accurate metallicity and velocity measurements even in distant GGCs. The brightest stars in the optical and IR in clusters older than $\approx 1$ Gyr are red giants, which are therefore the natural targets for precision measurements of cluster abundances and velocities. The CaT lines are extremely strong and near the peak flux of unreddened red giant branch (RGB) stars, and the technique only requires moderate resolution ($R \sim 3000$). Because there are many giants in a typical GC, the derived mean abundance can be determined much more robustly than that based on only one or a few stars. A reasonable sample of stars must be observed to ensure cluster membership, especially in bulge GCs (BGC) where membership on the bright RGB may be as low as 20–50% due to strong field contamination (Saviane et al. 2012). Observing in the near-infrared (NIR) is also very advantageous for reddened BGCs, where optical indices can be strongly absorbed. Many authors have confirmed the accuracy and repeatability of CaT abundance measurements in combination with broad-band optical photometry and shown its very high sensitivity to metallicity and insensitivity to age (e.g., Cole et al. 2004). Additionally, as reported by Carrera et al. (2013), the strength of the CaT lines depends mainly on iron abundances, and not on the Ca abundance, as has been pointed out also by several other investigations (e.g. Idiart et al. 1997; Battaglia et al. 2008).

In view of all of these advantages, in many GGCs a sample of their RGB stars has been observed using CaT. A seminal paper in this regard is that of Rutledge et al. (1997, R97). They observed a total of 976 giants in 52 GGCs and showed that the CaT is both a very efficient and accurate technique for deriving GC velocities and metallicities. Recently, Saviane et al. (2012, S12) began to complete CaT data for the large sample of GGCs remaining without such measurements. They obtained CaT abundances for 20 new GGCs. Still, this leaves more than one half of the GGCs without CaT data, including most BGCs. The BGC system is among the most important in our Galaxy and a thorough knowledge of metallicities and velocities can help to constrain bulge formation and evolution models. Nevertheless, substantial crowding or high and possibly variable reddening limited attempts of using even the CaT technique on many of these BGCs. One of the main reasons is the traditional CaT technique, although it nominally involves only observations in the NIR, also requires optical photometry to calibrate the metallicity. It is well known that the CaT lines, in addition to being very metallicity sensitive, also depend on effective temperature and especially luminosity, and these effects must be removed to properly derive the metallicity. Traditionally, this is achieved by defining a reduced EW (rEW or $W'$) for the sum of some combination of the three lines, which is then corrected for luminosity and temperature effects using the slope of the RGB, in particular, the magnitude difference in $V$ between the star and the horizontal branch (HB), $V_{HB} - V$. This differential method is very

powerful because it also removes any dependence on distance or mean reddening. Unfortunately, it also requires good optical photometry, which is often problematic for BGCs. Indeed, for many BGCs $V_{HB}$ is only very poorly known. Clearly, it would be very advantageous to develop a similar technique without these problems.

Here we establish a similar method in the IR, using as the fiducial magnitude the $K_s$ magnitude of the reddest part of the HB (RHB) or of the red clump (RC). This combines the power of the differential technique with the advantages of IR observations in minimizing extinction and reddening effects.

A major advantage of this work is the possibility of exploiting databases that are homogeneous both in terms of spectroscopy and photometry. Our photometric dataset consists of a catalog of GCs observed as part of the Vista Variables in the Via Lactea (VVV) Survey (Saito et al. 2012), calibrated on the system of the Two Micron All Sky Survey (2MASS, Skrutskie et al. 2006). This proves to be the ideal catalog for this purpose, since it is integrated with the 2MASS PSC. We used the spectroscopic dataset presented in S12, and also in R97, while we adopted the scale of Carretta et al. (2009) scale as the metallicity reference, which is based on UVES and GIRAFFE HR spectra.

We note that an initial attempt at involving NIR photometry to calibrate CaT was made by Olszewski et al. (1991), who used the absolute $I$ magnitude of the red giant to correct for luminosity and temperature effects. Unfortunately, this requires an accurate distance, which is certainly problematic for BGCs. Another attempt of calibrating the CaT in the NIR was made by Warren & Cole (2009) using spectra of 133 red giant stars from ten Galactic open clusters and two Galactic globular clusters, and the metallicity scale of Zinn & West (1984). They found a linear correlation. However, the scales of Zinn & West (1984) and Carretta et al. (2009) are not correlated properly by a simple linear relation, but by at least a quadratic expression. Previous works that used NIR photometry to correct for the CaT are Lane et al. (2010) and Warren & Cole (2009), but the former used the $K_s$ magnitude of the tip of the RGB as reference level, while the latter took the value of $K_s$ at the RR Lyrae instability strip for the GCs.

The CaT method can also be applied to derive the metallicity for red giants in any stellar population for which $V_{HB}$ is known, for instance dwarf spheroidal galaxies, the Magellanic Clouds, extragalactic globular clusters, or even M31 (Battaglia et al. 2011; Parisi et al. 2010; Foster et al. 2010; Jones et al. 1984; Cenarro et al. 2008). Adapting the technique to the IR allows us to apply it to any stellar population where reddening is problematic, which adds many targets for detailed study.

Here we first present our observations and reductions (Sect. 2). Next we present the metallicity calibration and discuss individual clusters (Sect. 3). Our conclusions are discussed in Sect. 4.

## 2. Observations and reductions

Our main target list consists of the GCs analyzed by S12. The NIR imaging collected in the context of the VVV Survey was used for all clusters included in the survey area. We also checked whether any of the GCs in the dataset not observed by the VVV Survey had useful 2MASS photometry, that would permit us to determine the RHB position. Including these GCs as well allowed us to better constrain the calibration over a wider metallicity range with better sampling. We similarly selected GCs from the R97 catalog to determine a calibration for this dataset as well. All clusters analyzed here are listed in Table 1. The complete

**Table 1.** List of RHB levels.

| ID | Photometric source | $K_s$(HB) | $\sigma$ |
|----|------|------|------|
| NGC 6380 | VVV | 13.80 | 0.05 |
| NGC 6440 | VVV | 13.64 | 0.05 |
| NGC 6441 | VVV | 14.38 | 0.05 |
| NGC 6522 | VVV | 13.16 | 0.05 |
| NGC 6528 | VVV | 13.11 | 0.05 |
| NGC 6544 | VVV | 10.50 | 0.05 |
| NGC 6553 | VVV | 12.27 | 0.05 |
| NGC 6558 | VVV | 13.30 | 0.10 |
| NGC 6569 | VVV | 14.30 | 0.05 |
| NGC 6624 | VVV | 13.28 | 0.05 |
| NGC 6626 | VVV | 13.00 | 0.05 |
| NGC 6637 | VVV | 13.51 | 0.05 |
| NGC 6638 | VVV | 13.70 | 0.05 |
| NGC 6656 | VVV | 11.70 | 0.10 |
| NGC 2808 | 2MASS | 14.02 | 0.05 |
| NGC 3201 | 2MASS | 12.05 | 0.10 |
| NGC 4372 | 2MASS | 12.05 | 0.20 |
| NGC 4590 | 2MASS | 13.30 | 0.20 |
| NGC 6121 | 2MASS | 9.97 | 0.05 |
| NGC 6139 | 2MASS | 13.75 | 0.15 |
| NGC 6254 | 2MASS | 11.87 | 0.05 |
| NGC 6325 | 2MASS | 13.27 | 0.05 |
| NGC 6356 | 2MASS | 14.60 | 0.05 |
| NGC 6397 | 2MASS | 10.45 | 0.05 |
| NGC 6541 | 2MASS | 13.00 | 0.20 |
| NGC 6809 | 2MASS | 12.00 | 0.20 |
| NGC 6838 | 2MASS | 11.78 | 0.05 |
| NGC 7078 | 2MASS | 13.50 | 0.10 |
| NGC 7099 | 2MASS | 13.40 | 0.15 |
| Pal 7 | 2MASS | 12.55 | 0.05 |

data for all spectroscopic stars are presented in Table 8, and the metallicity values are listed in Tables 2–7, separately for each spectroscopic dataset.

## 2.1. Spectroscopy

### 2.1.1. S12 data

The data were obtained in the *z*-band region of giant stars with FORS2 (Appenzeller et al. 1998), installed at the Cassegrain focus of VLT/UT1-Antu. The approach used to assemble the list of clusters observed is discussed in S12. All spectra were extracted using the FORS2 pipeline version 1.2 (Izzo et al. 2010). The absorption lines of the CaT were used both to measure radial velocities and derive metallicities. Metal-rich clusters were measured with Gaussian plus Lorentzian function fits, while the equivalent widths for metal-poor clusters were computed with Gaussian fits alone and were transformed onto the scale established in Gullieuszik et al. (2009, G09). This decision is justified because we verified that there is a one-to-one correspondence between widths measured with the two methods.

The final $\Sigma W_{S12}$ for each star results from the sum of the EWs of the two strongest CaT lines (8542 Å, 8662 Å):

$$\Sigma W_{S12} = EW(8542\text{ Å}) + EW(8662\text{ Å}). \qquad (1)$$

We refer to S12 for a more complete description of the observations, reduction procedure, and selection for cluster membership.

### 2.1.2. R97 data

We also retrieved the spectroscopic data from Rutledge et al. (1997, R97). Not all of the clusters in R97 were used because

of the difficulty of identifying the stars in the scanned finding charts. We included all the more metal-poor and metal-rich GCs, those included in the VVV Survey, and others to properly cover the full metallicity range of GGCs.

In this case the final $\Sigma W$ for each star is the weighted sum of the three CaT lines:

$$\Sigma W_{R97} = 0.5 \cdot EW(8498\text{ Å})$$
$$+ EW(8542\text{ Å}) + 0.6 \cdot EW(8662\text{ Å}). \qquad (2)$$

We refer to R97 for a more complete description of the observations, reduction procedure, and selection for cluster membership.

## 2.2. Photometry

The VVV Survey (Minniti et al. 2010; Catelan et al. 2011) is one of six ESO Public Surveys carried out at the four-meter Visible and Infrared Survey Telescope for Astronomy (VISTA), which scans the Galactic bulge ($-10 \leq l \leq +10$, $-10 \leq b \leq +5$) and the adjacent part of the southern disk ($-65 \leq l \leq -10$, $-2 \leq b \leq +2$). The survey collects data in five NIR bands ($ZYJHK_s$) with the VIRCAM camera (Emerson & Sutherland 2010), an array of sixteen $2048 \times 2048$ pixel detectors with a pixel scale of $0.''341$/pix. VVV images extend to several magnitudes fainter than those of 2MASS, and have a higher increased spatial resolution (Saito et al. 2010). These two factors are particularly important for mitigating contaminated photometry in crowded regions near the Galactic center and the cores of globular clusters. The VVV survey provides precise multi-epoch $K$-photometry for 39 GGCs, which permits obtaining $K_s$ magnitudes with good accuracy. For this reason, we preferred $K_s$ magnitudes over of $J$ or $H$ ones, to correct the equivalent widths.

We retrieved the VVV images containing the GGCs targeted by S12 and R97 from the Vista Science Archive website[1], pre-reduced at the Cambridge Astronomical Survey Unit (CASU)[2] with the VIRCAM pipeline (Irwin et al. 2004). We performed photometry through fitting of point spread function using the VVV-SkZ_pipeline code (Mauro et al. 2013), which is based on DAOPHOT suite (Stetson 1987, 1994), on the single $2048 \times 2048$ pixel chips extracted from the stacked VVV pawprints (Saito et al. 2012). The photometry was tied to the 2MASS system, as described in Moni Bidin et al. (2011) and Chené et al. (2012). The use of the 2MASS system as the standard photometric system permitted us to integrate our photometric database with the 2MASS PSC. The use of the VVV-SkZ_pipeline was fundamental for this work, since it is the only photometric procedure for VVV data that provides accurate photometry even for partially saturated stars, which most of the giants observed spectroscopically are. As can be seen in Fig. 1, almost 90% of the observed stars are brighter than the saturation limit for the VVV survey ($K_s = 12$), but our photometry is still reliable up to $K_s = 9$–10, as the comparison with 2MASS photometry in Fig. 2 shows.

The stars with spectroscopic CaT measurements were identified in our VVV photometry. In some cases it was not possible to find a corresponding star in the VVV catalogs, that is, very bright stars ($K_s < 9$) completely saturated on the VVV images. It this case, their photometric data were obtained from the 2MASS PSC catalog. The GC HP1 was excluded due to the difficulty in identifying the cluster RHB. The data for all spectroscopic stars are presented in Table 8, which is only available at the CDS.
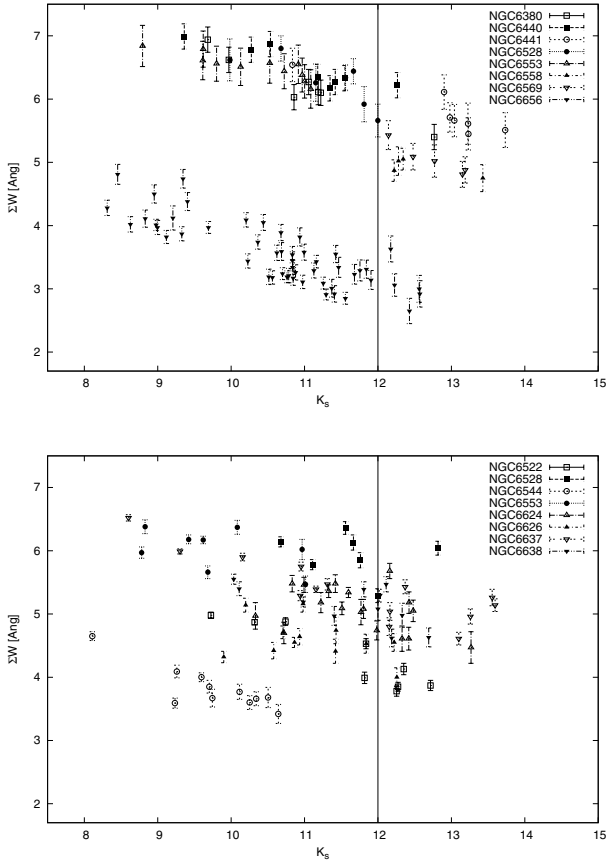
---

**Fig. 1.** Ca II line strength plotted against $K_s$ magnitude for VVV clusters in S12 and R97 catalogs. The vertical bold line at $K_s = 12$ is the saturation limit for the VVV survey. Vertical bars on each point show the measurement uncertainty in the line strengths. The measurement uncertainty in magnitude is too small to be noticed.
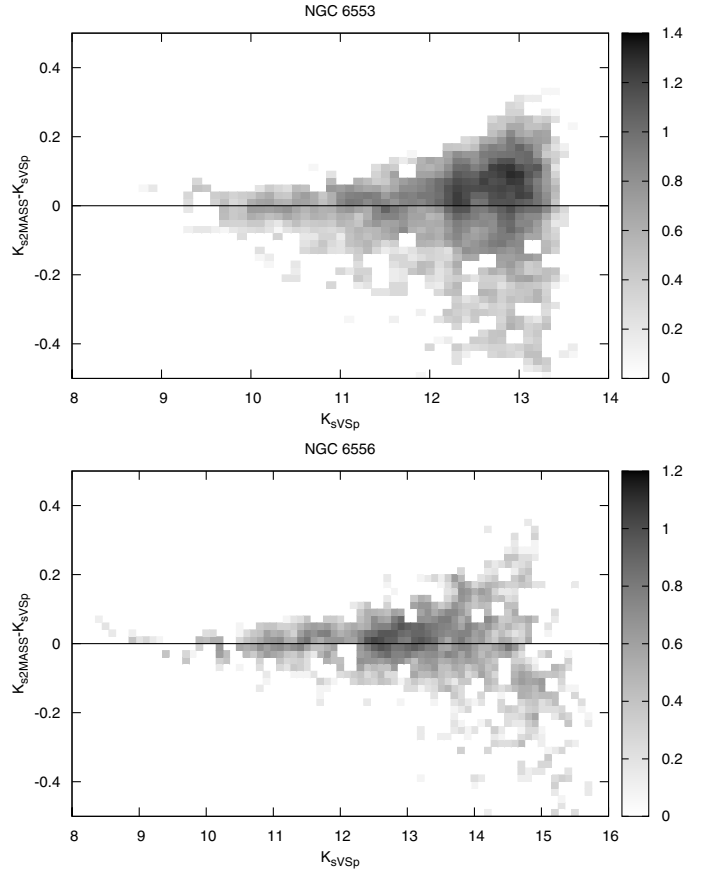


**Fig. 2.** Density map in logarithmic scale of the photometric differences in $K_s$ between 2MASS and VSp catalogs, as a function of $K_s$ magnitude obtained with the VVV-SkZ_pipeline (VSp, upper figure for NGC 6553, lower figure for NGC 6656). No systematic offset exists, especially for the brighter ($K_s < 12$) stars, which are saturated in the VVV data.

### 2.2.1. Determining the HB-level magnitude

The magnitude at the HB level was determined by the position of the peak in the luminosity distribution of the reddest part of the HB. The HB of some metal-poor GCs (like NGC 6121, NGC 6397, or NGC 6809) is well populated also at the red end, which permits an accurate determination of the RHB magnitude. For most of the metal-poor GCs, however, the red HB is not easily detectable in the color–magnitude diagram (CMD). We determined theoretically a "first-guess" position of the RHB in these cases, and compared it with the peaks in the luminosity distribution for the stars located along and next to the RGB, 2–3′ from the cluster center. We used the metal-poor GCs with well defined RHB to calibrate this procedure. We determined the initial position by considering the results given by several procedures. We calculated a "theoretical" value based on Bressan et al. (2012) and Girardi & Salaris (2001), corrected for distance modulus and reddening of the GC. An empirical value was also calculated from the $V_{HB}$ value listed in Harris (1996, 2010 edition, hereafter H10), corrected for distance modulus and reddening of the GC, for a mean $(V - K_s)$ color taken from Bressan et al. (2012). The accuracy of these two methods strongly depends on the accuracy of the photometric parameters of the cluster. The CaT datasets also include the $\Delta V = V_{HB} - V$ for each star; we fitted the points in the $(\Delta V; K_s)$ plane with linear and quadratic[3]

---

[3] The locus of the points in the $(V_{HB} - V; K_s)$ plane is not perfectly linear, but slightly convex.

relations: the intercepts give an estimate of the $K_s$ magnitude of RGB stars that in the optical have the same luminosity of the RHB. We noted that this method can have an uncertainty as large as 0.5 mag and strongly depends on the accuracy of $V_{HB}$ and on the magnitude range covered by the data. We used these estimates, together with the values presented in Valenti et al. (2007, 2010), as an initial position to identify RHB among the peaks in the $K_s$ luminosity distribution. Additionally, we used the empirical calibration for the RGB bump (Valenti et al. 2007) applied to the parameters listed in H10 to determine the position of the bump in the luminosity distribution, to avoid confusion between the peaks associated with the two different features. The results are presented in Table 1.

The comparison between our $K_s$(HB) values and those deduced from the $(V(HB) - V; K_s)$ fit suggests that the value of $V_{HB}$ is not very accurate for most of the faintest GCs. In fact, 73% of GCs with $K_s$(HB) < 13 agree between the two values within 0.2 mag, but this fraction reduces to 37% among fainter GCs.

### 2.3. Metallicities

The metallicities were taken from Carretta et al. (2009, hereafter C09), who measured [Fe/H] for 19 GCs from the analysis of spectra of about 2000 RGB stars using FLAMES/VLT (about 100 stars with GIRAFFE and about 10 with UVES, respectively, in each GC). With these data, they recalibrated their

previous metallicity scale (e.g. Carretta & Gratton 1997, CG97) to the UVES scale, giving the calibration relations, and assembled a table of [Fe/H] values for 133 clusters present in the catalog of Harris (1996). The metallicities were computed based on the weighted average of indices published in four different studies, putting them on a single UVES scale. These values are reliable, but they were not obtained from spectroscopic analysis for all the clusters. Nevertheless, C09 has the advantage of being a homogeneous metallicity scale, and it is the main metallicity source for H10. We considered for the calibration only the values not derived from Harris (1996) (clusters with a "1" in the Notes column of Appendix 1 of C09). The S12 dataset includes eight of the GCs used in C09 as calibrators (NGC 2808, NGC 3201, NGC 6121, NGC 6254, NGC 6397, NGC 6441, NGC 6838, and NGC 7078), while seven calibrators (NGC 2808, NGC 3201, NGC 4590, NGC 6121, NGC 6397, NGC 6809, and NGC7099) are taken from the R97 sample used in this work.

We observed that, while the majority of GCs in the ([Fe/H]$_{C09}$; $\langle W' \rangle$) plane lie within $\sim 1\sigma$ to the fit, others (namely NGC 6528, NGC 6558 and NGC 6569) present larger differences. These clusters are not part of the 19 C09 calibrators, and their metallicities were derived through the weighted average of literature values. Checking the sources of the metallicities for these three objects, we found that NGC 6528 and NGC 6558 have recent HR spectroscopic metallicities in poor agreement with the C09 metallicity. H10 reported four sources of HR spectroscopic metallicity for NGC 6528. Carretta et al. (2001) based their estimate on observations carried out with the High Resolution Echelle Spectrometer (HIRES) at *Keck* I (final $R \approx 15\,000$) of four HB stars. The estimate of Origlia et al. (2005) is based on IR echelle spectra of four bright core giants, acquired with the IR spectrograph NIRSPEC ($R \sim 25\,000$) mounted at the *Keck* II Telescope. The other two are based on the same spectra acquired by Zoccali et al. (2004) with UVES ($R \sim 45\,000$–$55\,000$) of three stars (one HB star and two red giants). While the metallicity derived by Carretta et al. (2001) (and used in C09) is $+0.07 \pm 0.08$ dex, the Origlia et al. (2005) NIRSPEC metallicity is $-0.17 \pm 0.01$ dex, and the UVES value is $-0.1 \pm 0.2$ dex and $-0.24 \pm 0.19$ dex, from Zoccali et al. (2004) and Sobeck et al. (2006), respectively. The photometric estimates obtained by Momany et al. (2003) are centered on the mean of field stars in Baade's Window, [Fe/H] $= -0.25$, as derived by McWilliam & Rich (1994). We note that the metallicity distributions of the stars in the S12 and R97 catalogs of this GC, according to our calibrations, are both almost flat, covering a metallicity range of $\approx 1$ dex. For NGC 6558, Barbuy et al. (2007) estimated a metallicity of $-0.97 \pm 0.15$ dex, based on the analysis of HR spectra of five giant stars (two are in common with our sample) acquired at the VLT with the multifiber spectrograph FLAMES in GIRAFFE mode ($R \sim 22\,000$). C09 demonstrated that the metallicity scales obtained with UVES and GIRAFFE do not present systematic differences[4]. For NGC 6569, Valenti et al. (2011) found a metallicity of $-0.79 \pm 0.02$ dex, based on six HR IR echelle spectra acquired with NIRSPEC ($R \sim 25\,000$). The CG97 metallicity on the UVES/C09 scale is $-0.90$ dex, similar to the averaged photometric value of [Fe/H] $= -0.88$ dex estimated in Valenti et al. (2005). For the R97 dataset, NGC 6624 presents recent HR spectroscopic metallicities that poorly agree with the C09 metallicity and a difference with our best fits of more than $2\sigma$. NGC 6624 was analyzed with HR spectra in

Valenti et al. (2011), where they found [Fe/H] $= -0.69$ dex. Our calibration yields metallicity values on the scale of C09 that better agree with the metallicities estimated with HR spectroscopy than with the metallicities of C09, suggesting that the C09 estimates for these GCs may have problems. Based on these considerations, we decided to construct a second metallicity scale called "corrected C09" (C09c) to determine whether these more recent values provide a better calibration relation. For NGC 6626, which was not used as a calibration cluster, we used the value [Fe/H] $= -1.28$ dex for C09c calculated by Da Costa & Armandroff (1995) through the CaT method, as comparison.

We additionally calculated the calibration relations for the metallicities given in H10, since it is a commonly used source. All the metallicity values are listed in Tables 2–7.

## 2.4. Dependence of He abundance and contamination from AGB stars

Saviane et al. (2012) highlighted that the CaT method works on the assumption that $V_{HB}$ depends almost exclusively on [Fe/H], the other stellar parameters playing only a secondary role. While this is true for the age of old stellar systems such as GGCs (Salaris & Girardi 2002; Ferraro et al. 2006), cluster-to-cluster differences in helium abundance can instead be significant, and might cause higher residuals in the calibration, if these differences are not correlated with metallicity. In general, halo GGCs share a common He abundance (Buzzoni et al. 1983; Zoccali et al. 2000; Cassisi et al. 2003), but this might be different for BGCs. Nataf et al. (2013) recently postulated that bulge stars have a He enhancement $\Delta Y = 0.06$ with respect to halo GCs (see also Renzini 1994) to explain the difference between the luminosity of the RGB bump of the Galactic bulge and that predicted by the luminosity-metallicity relation of GGCs. S12 concluded that the cluster-to-cluster scatter in He content is not expected to affect the results of the CaT method, and we refer to their analysis for more details. We expect a similar behavior for $K_s$(HB), and the small scatter that the C09 calibrator GCs have around the fitting curves confirms this expectation.

Another potential concern is that, particularly in the differentially reddened clusters, the possibility that AGB stars are included in the selected RGB samples may lead to additional scatter in the ($\Sigma W$, $K_s - K_s$(HB)) plane, and thus to increased uncertainty in the derived abundances. On the other hand, this effect is expected to be quite small ($\Delta W = 0.04$ Å), as shown by Cole et al. (2000).

## 3. Results

Assuming the relation

$$\Sigma W = a[K_s(HB) - K_s] + W', \tag{3}$$

the slope $a$ is calculated through a least-squares fit[5], with the constraint that it must be the same for all the clusters. To a good approximation, the slope is independent of metallicity within the range spanned by our GCs.

Subsequently, we calculated $W'$ for all stars in each cluster, empirically removing the EW dependence on the star's gravity and temperature. We calculated $\langle W' \rangle$ for each GC, through a weighted average of $W'$ of all stars. We preferred this approach

---

[4] Mean difference "UVES minus GIRAFFE" of $-0.015 \pm 0.008$ dex with a rms scatter of 0.037 dex from 19 of their GCs.

[5] The algorithm is based on a series of five lectures presented at "V Escola Avançada de Astrofísica" by Peter B. Stetson; see `http://ned.ipac.caltech.edu/level5/Stetson/Stetson_contents.html`

**Fig. 4.** Calibration relations between [Fe/H] on the scale of C09 and NIR $\langle W' \rangle$ on the scale of G09.
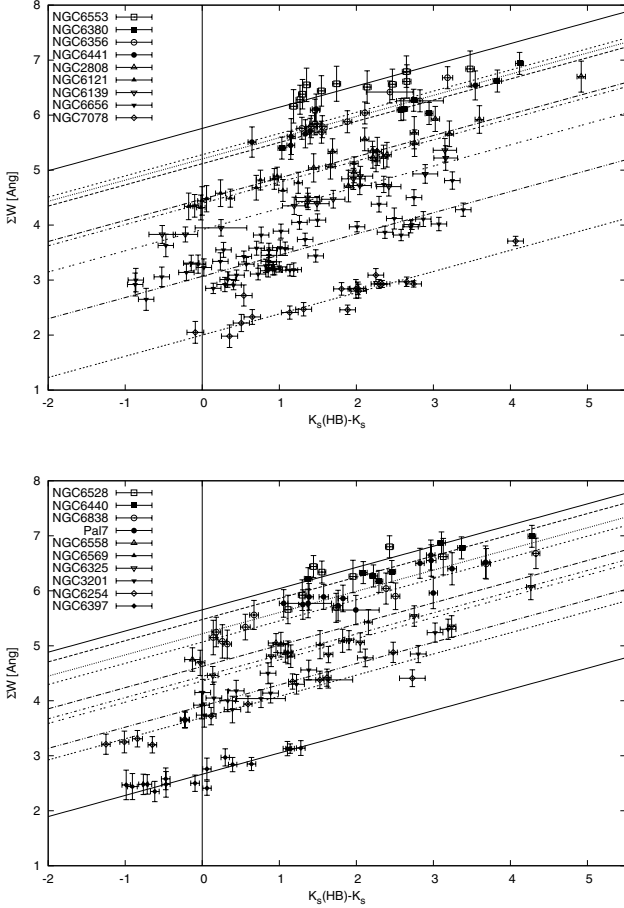


**Fig. 3.** Summed Ca II line strength $\sum W_{S12}$ plotted against magnitude difference from the red clump $K_s(\mathrm{HB}) - K_s$ for the selected clusters. The data for each cluster were fit with a line of slope $-0.385$ Å/mag with a urms of 0.013 Å/mag. The data were split to avoid too much overlap.

**Fig. 5.** Calibration relations between [Fe/H] on the scale of corrected C09 and NIR $\langle W' \rangle$ on the scale of G09.

instead of the intercept value provided by the least-squares fit method because, while the two estimates differ very little, the uncertainties associated with the fit heavily depend on the number of data, and are thus overestimated. Finally, the [Fe/H] vs. $\langle W' \rangle$ relation was calculated for each metallicity scale with a polynomial fit to define the best calibration relation. The unbiased residual mean square (hereafter urms or $\sigma$) was assumed as the uncertainty of our fit. It consists of the square root of the sum of the square of the residuals, divided by the number of degrees of freedom for error[6], instead of the number of data points, so that we can remove the bias on the estimate of the variance of the unobserved errors.

### 3.1. Calibration of reduced equivalent widths from S12

The $\sum W_{S12}$ values are plotted vs. $K_s(\mathrm{RHB}) - K_s$ in Fig. 3. For the slope we obtain $a = -0.385$ Å/mag with a urms of 0.013 Å/mag. The $\langle W' \rangle$ cover a range of 2–5.8 Å.

The calibration relations for [Fe/H] on the scale of C09 and the NIR $\langle W' \rangle$ on the scale of G09 are shown in Fig. 4, defined in a [Fe/H] range from $-2.33$ dex to $+0.07$ dex. As can be seen in the figure, both the cubic and the quadratic

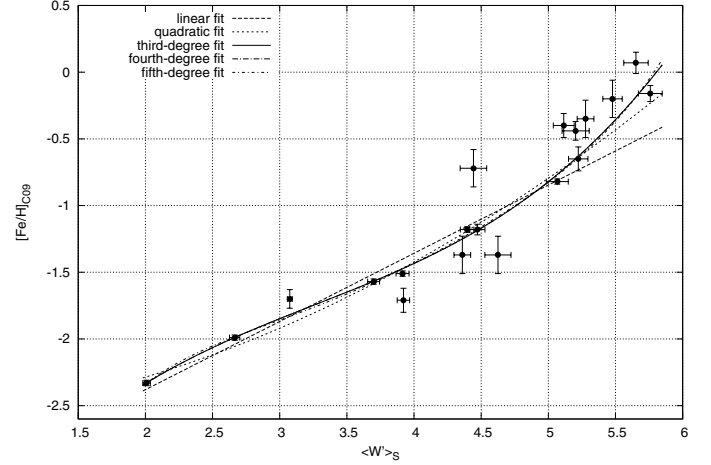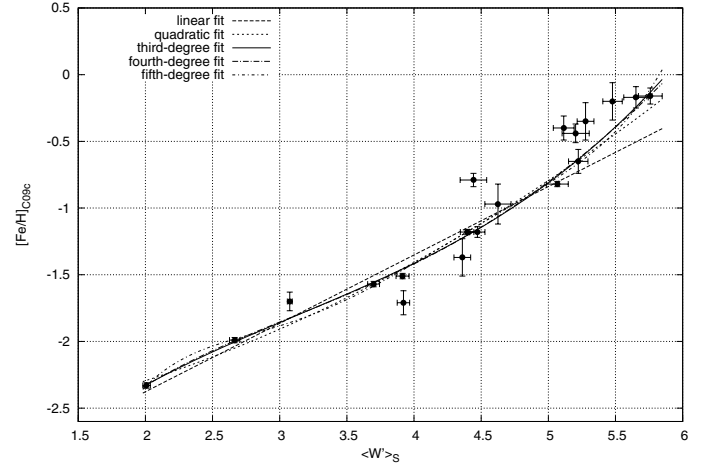relations reproduce the observed trend well, while the linear relation does not fit the more metal-rich GCs properly. The fourth- and fifth-order polynomials do not differ noticeably from the third-order polynomial. The cubic calibration relation is

$$[\mathrm{Fe/H}]_{\mathrm{C09}} = -4.61 + 1.842\langle W' \rangle - 0.4428\langle W' \rangle^2 + 0.04517\langle W' \rangle^3, \quad (4)$$

with a urms of 0.214 dex (0.113 dex considering only the 8 GCs used as calibrators in C09). The quadratic calibration relation

$$[\mathrm{Fe/H}]_{\mathrm{C09}} = -2.63 + 0.040\langle W' \rangle + 0.0653\langle W' \rangle^2, \quad (5)$$

with a urms of 0.237 dex (0.110 dex considering only the 8 calibrators). The differences in metallicity between the cubic and the quadratic fit are smaller than 0.1 dex in absolute value in the range of definition ($2 < \langle W' \rangle < 5.5$, $-2.3 < [\mathrm{Fe/H}] < -0.3$), increasing to 0.35 for $\langle W' \rangle = 6$ ([Fe/H] $\sim 0.1$).

The calibration relations for [Fe/H] on the scale of C09c and the NIR $\langle W' \rangle$ on the scale of G09 are shown in Fig. 5. They are defined over an [Fe/H] range from $-2.33$ dex to $-0.17$ dex. The differences between the cubic and quadratic calibration relations are slightly smaller than for the scale of C09. The cubic calibration relation in this revised system is

$$\begin{aligned}[\mathrm{Fe/H}]_{\mathrm{C09c}} = {}& -4.09 + 1.341\langle W' \rangle \\ & -0.2919\langle W' \rangle^2 + 0.03098\langle W' \rangle^3, \quad (6)\end{aligned}$$

---

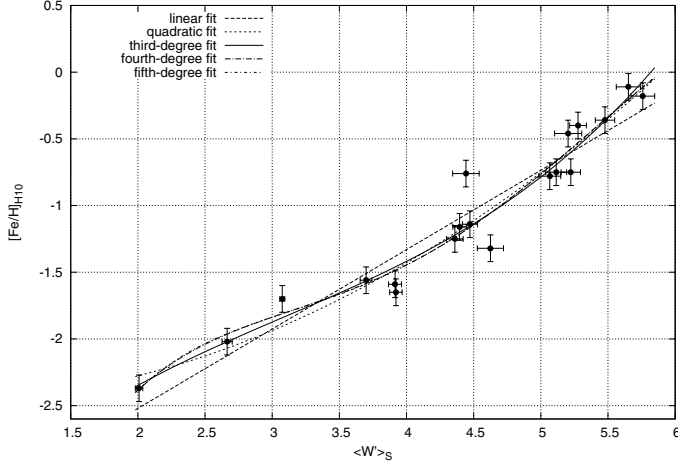[6] The number of data points minus the number of the coefficients of the curve used to fit them.

**Fig. 6.** Calibration relations between [Fe/H] on the scale of H10 and NIR $\langle W' \rangle$ on the scale of G09.



**Fig. 7.** Comparison of the cubic calibration relations [Fe/H] vs. NIR $\langle W' \rangle$ on the scale of G09 in the three metallicity scales and the one obtained in S12 for the visible.

with a urms of 0.173 dex (0.114 dex considering only the eight calibrators). The quadratic calibration relation reads

$$[\text{Fe/H}]_{\text{C09c}} = -2.73 + 0.103\langle W' \rangle + 0.0568\langle W' \rangle^2, \tag{7}$$

with a urms of 0.180 dex (0.110 dex considering only the eight calibrators).

The calibration relations for [Fe/H] on the scale of H10 and the NIR $\langle W' \rangle$ on the scale of G09 are shown in Fig. 6. They are defined over an [Fe/H] range from $-2.37$ dex to $-0.11$ dex. The differences between the cubic and quadratic calibration relations are slightly smaller than for the scales of C09. The cubic calibration relation is

$$\begin{aligned}[\text{Fe/H}]_{\text{H10}} &= -4.14 + 1.371\langle W' \rangle \\ &\quad - 0.3032\langle W' \rangle^2 + 0.03263\langle W' \rangle^3, \end{aligned} \tag{8}$$

with a urms of 0.165 dex. The quadratic calibration relation is

$$[\text{Fe/H}]_{\text{H10}} = -2.45 - 0.080\langle W' \rangle + 0.0839\langle W' \rangle^2, \tag{9}$$

with a urms of 0.165 dex.

### 3.1.1. Comparison between reference scales

We compared the three calibration relations for the S12 dataset obtained in this study with the one calculated at optical wavelengths in S12. The cubic and the quadratic fits do not differ noticeably, and S12 presented a cubic relation, hence the third-order solution was adopted in the comparison. As can be seen in Fig. 7, the four relations are approximately the same, with differences smaller than 0.1 dex over the whole metallicity range. The three relations from this work differ among each other by generally less than 0.02–0.04 dex, with a highest value of 0.08 dex between the solutions C09 and C09c at the metal-rich end. This demonstrates that the three scales are approximately the same, and the lowest values of urms may indicate a more precise calibration. This overall comparison demonstrates that the photometric correction to the CaT equivalent widths is independent of the passband used, since the same calibration relation can be adopted when using both optical and NIR magnitudes. Additionally, the good agreement over the whole metallicity range demonstrates that the HB level was determined with sufficient accuracy in our work.
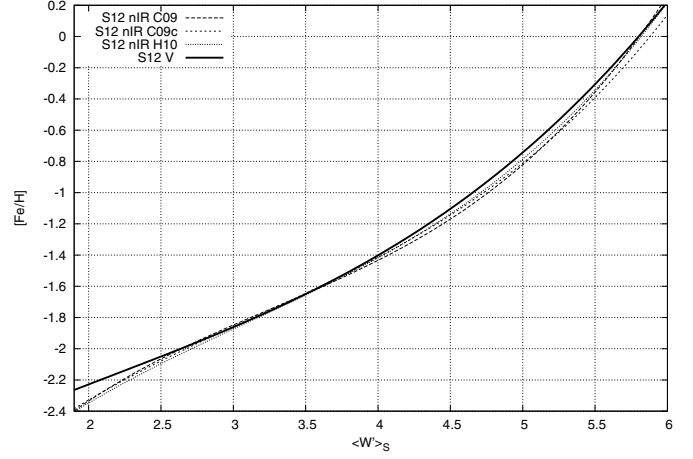
Comparing the C09 metallicities with those obtained from our equation (see Table 2), six of the 19 GCs present a difference larger than $1\sigma$. However, the metallicity of three of these is controversial, and is poorly known for the other two. Only NGC 6569 among these GCs presents a difference larger than $2\sigma$. We derived a metallicity of $-1.20$ dex for it, similar to those of NGC 2808 and NGC 6121, versus the C09 value of $-0.72$ dex. We get [Fe/H] $= -0.58$ dex (instead of $-0.35$ dex) for NGC 6356, $-0.19$ dex (instead of $+0.07$ dex) for NGC 6528, and $-1.09$ dex (instead of $-1.37$ dex) for NGC 6558. For the two GCs with poorly known metallicity, the equation gives $-1.47$ dex for NGC 6139 (C09 suggests $-1.71$ dex), and $-0.73$ dex for NGC 6380 ($-0.40$ dex). The statistic is similar in the comparison with the scale of C09c (see Table 3): 6 GCs with $|\Delta[\text{Fe/H}]| > 1\sigma$, with NGC 6569 still the only one with $|\Delta[\text{Fe/H}]| > 2\sigma$. We now obtain a difference smaller than $1\sigma$ for NGC 6528 and NGC 6558, while the discrepancy for NGC 6440 and NGC 6441 is now larger than before: the equation gives $-0.41$ dex (against the C09 value of $-0.20$ dex), and $-0.65$ dex ($-0.44$ dex), respectively. We note that, in these two C09-based scales, NGC 6441 is the only one of the eight C09 calibrators that presents a $\Delta[\text{Fe/H}] > 0.3\sigma$. For the H10 scale (see Table 4), only four of the 19 GCs present $|\Delta[\text{Fe/H}]| > 1\sigma$, namely NGC 6139, NGC 6558, NGC 6569, and NGC 6656 ($-1.90$ dex instead of $-1.70$ dex).

### 3.2. Calibration of reduced equivalent widths from R97

The $\Sigma W_{R97}$ values are plotted vs. $K_s - K_s$RHB in Fig. 8. For the R97 dataset we obtain $a = -0.380$ Å/mag with a urms of 0.014 Å/mag. This value differs from the one for S12 by only 0.005 Å/mag ($\approx 0.4\sigma$), consequently, the slope is independent of the way the equivalent width is calculated. Such variation would cause a change in the mean rEW of less than 0.02 Å in our case, which is completely negligible. The $\langle W' \rangle$ cover a range of 1.6–5.1 Å.

The calibration relations for [Fe/H] on the scale of C09 and the NIR $\langle W' \rangle$ are shown in Fig. 9, defined over an [Fe/H] range from $-2.33$ dex to $+0.07$ dex. The calibrations based on a fourth- and fifth-order polynomial are not suitable, and consequently were rejected. The best fits are obtained with the cubic and
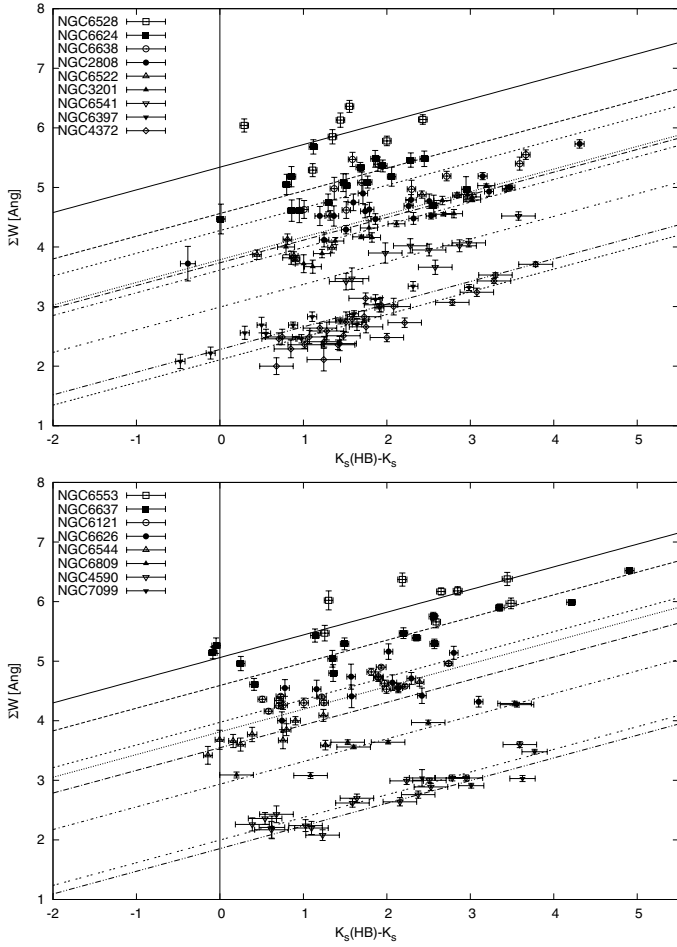
**Fig. 8.** Summed Ca II line strength ($\sum W_{R97}$) plotted against magnitude difference from the red clump $K_s(\text{RHB}) - K_s$ for the selected clusters. The data for each cluster were fit with a line of slope $-0.348$ Å/mag. The data were split to avoid too much overlap.



**Fig. 9.** Calibration relations between [Fe/H] on the scale of C09 and NIR $\langle W' \rangle$ on the scale of R97.



**Fig. 10.** Calibration relations between [Fe/H] on the "corrected C09" scale and NIR $\langle W' \rangle$ on the scale of R97.

quadratic relations, while the linear one does not fit the more metal-rich GCs properly, as observed also for the S12 dataset, or the more metal-poor GCs. The quadratic calibration relation is

$$[\text{Fe/H}]_{\text{C09}} = -2.24 - 0.254\langle W' \rangle + 0.13094\langle W' \rangle^2, \tag{10}$$

with a urms of 0.102 dex (0.114 dex considering only the seven GCs used as calibrators in C09), while the cubic calibration relation is

$$[\text{Fe/H}]_{\text{C09}} = -2.90 + 0.393\langle W' \rangle$$
$$-0.0684\langle W' \rangle^2 + 0.01939\langle W' \rangle^3, \tag{11}$$

with a urms of 0.113 dex (0.130 dex considering only the seven calibrators). The differences in metallicity between the cubic and the quadratic fits are smaller than 0.06 dex in absolute values in almost the entire range of definition ($1.7 < \langle W' \rangle < 5.0$, $-2.2 < [\text{Fe/H}] < -0.3$), increasing to 0.2 for $\langle W' \rangle = 5.3$ ($[\text{Fe/H}] \sim 0.0$).

The calibration relations for [Fe/H] on the scale of C09c and the NIR $\langle W' \rangle$ are shown in Fig. 10. They are defined over an [Fe/H] range from $-2.33$ dex to $-0.16$ dex. The differences between the cubic and quadratic calibration relations are slightly smaller than for the scale of C09. The quadratic calibration relation is

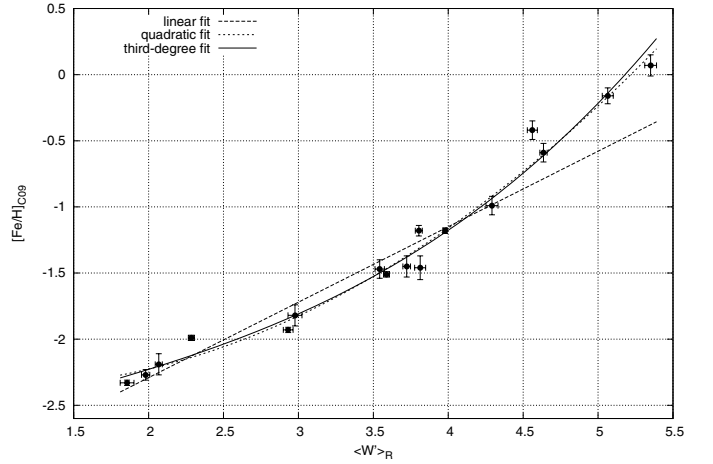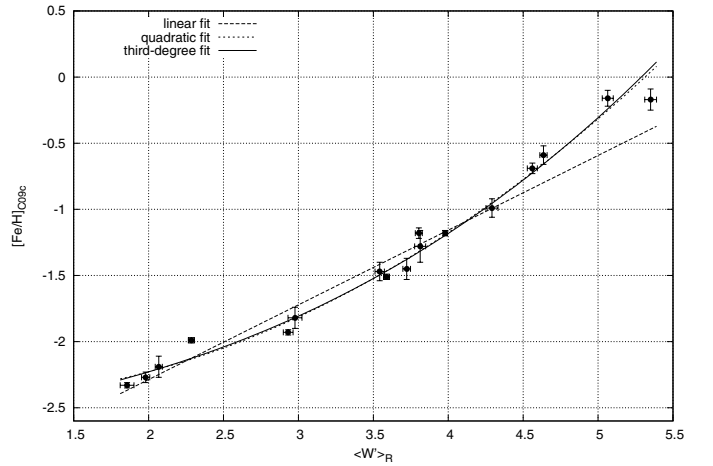$$[\text{Fe/H}]_{\text{C09c}} = -2.39 - 0.143\langle W' \rangle + 0.1116\langle W' \rangle^2, \tag{12}$$

with a urms of 0.096 dex (0.115 dex considering only the seven calibrators). The cubic calibration relation is

$$[\text{Fe/H}]_{\text{C09c}} = -2.66 + 0.125\langle W' \rangle$$
$$+0.0285\langle W' \rangle + 0.00809\langle W' \rangle^3, \tag{13}$$

with a urms of 0.104 dex (0.133 dex considering only the seven calibrators).

The calibration relations for [Fe/H] on the scale of H10 and the NIR $\langle W' \rangle$ are shown in Fig. 11. They are defined over an [Fe/H] range from $-2.27$ dex to $-0.11$ dex. The differences between the cubic and quadratic calibration relations are smaller than 0.06 dex in the whole range. The quadratic calibration relation is

$$[\text{Fe/H}]_{\text{H10}} = -2.53 - 0.037\langle W' \rangle + 0.09658\langle W' \rangle^2 \tag{14}$$

and has a urms dispersion around the fit of 0.110 dex. The cubic calibration relation is

$$[\text{Fe/H}]_{\text{H10}} = -0.66 - 1.821\langle W' \rangle$$
$$+0.6211\langle W' \rangle^2 - 0.04848\langle W' \rangle^3 \tag{15}$$
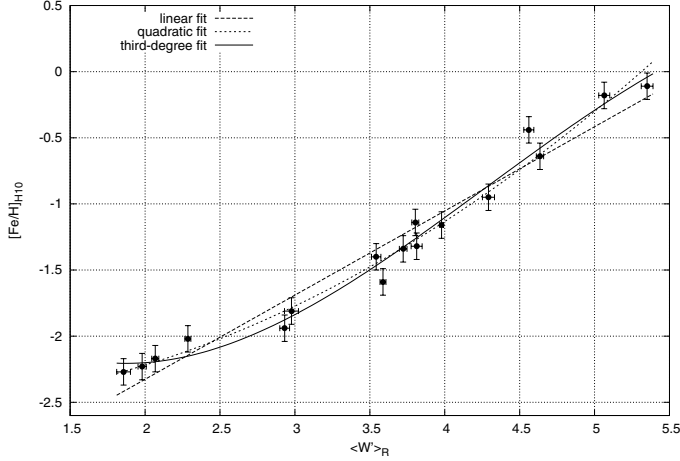
and has a urms dispersion around the fit of 0.103 dex.

**Fig. 11.** Calibration relations between [Fe/H] on the scale of H10 and NIR $\langle W' \rangle$ on the scale of R97.

### 3.2.1. Comparison between the reference scales

For the comparison between the three metallicity scales, we chose to use the quadratic relations, since they have lower urms values. Our three relations are approximately the same, even for this dataset, as can be seen in Fig. 12. The differences are negligible, are smaller than ~0.03 dex over most of the metallicity range, with a highest value of 0.08 dex at the more metal-rich GCs. The relation of H10 presents a systematic overestimate of ~0.04 dex compared with the other two.

The linear relation between the $V$-band rEW and [Fe/H] presented by C09 was defined in the ranges $1.5 < \langle W' \rangle < 4.7$ and $-2.33 < [Fe/H] < -0.7$, thus excluding the most metal-rich GCs. As can be noted in Figs. 9–11, in this metallicity range the difference among the cubic and quadratic fits and the linear one is $\lesssim 1\sigma$. When we recalculate the urms for our linear fits in the same metallicity range, we obtain results more similar to the urms of the quadratic equation (0.116, 0.099, and 0.149 dex, respectively for the three scales), showing that a nonlinear fit is needed that also includes the metal-rich end. We compared both the quadratic and the linear calibration relations for the NIR rEW with those from C09. While the quadratic relations present an obvious difference with the optical one, the comparison among the four linear relations (see lower plot in Fig. 12) confirms that the ([Fe/H] vs. rEW) relation can be considered to be almost independent of the passband used for the photometry.

Comparing the metallicities of C09 with those obtained from our equations (see Table 5), the quadratic equation yields a metallicity different by more than $1\sigma$ for four GCs, namely NGC 2808, NGC 6397, NGC 6624, and NGC 6626. The problems related to the controversial metallicity of the last two GCs were already discussed in Sect. 2.3. The cubic solution gives a difference $\Delta[Fe/H] > 1\sigma$ even for NGC 6528. NGC 6624 is the only cluster with $\Delta[Fe/H] > 2\sigma$, with an estimated metallicity of $-0.67$ dex, compared with the value of C09 of $-0.42$ dex. We obtain [Fe/H] $= -1.31$ dex for NGC 2808, while C09 gives $-1.18$ dex and S12 equation ~$-1.14$ dex, $-2.14$ dex for NGC 6397, versus $-1.99$ dex, for both C09 and S12 equation, and $-1.31$ dex for NGC 6626, instead of $-1.46$ dex. Considering the six GCs in common with the dataset of S12, the metallicity obtained for NGC 3201 and NGC 6121 perfectly agree, while NGC 6553 presents a difference $\Delta[Fe/H] \approx 1\sigma$. NGC 6528 shows an even larger discrepancy, but its metallicity is controversial and, along with NGC 6553, it is sensitive to the fit
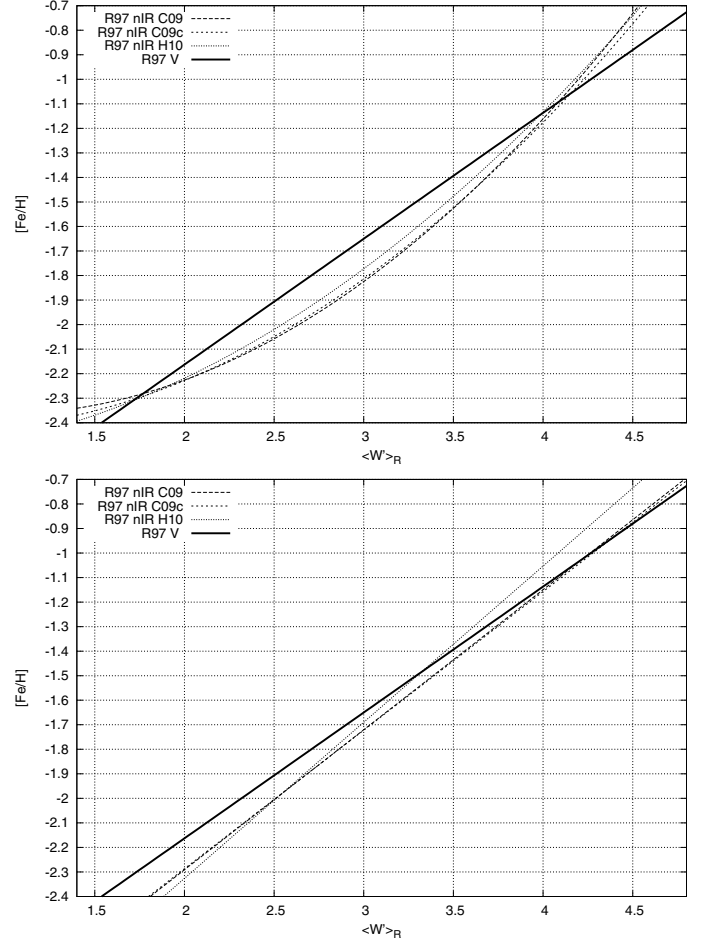


**Fig. 12.** Comparison between the quadratic (*upper panel*) and linear (*lower panel*) calibration relations [Fe/H] vs. NIR $\langle W' \rangle$ on the three metallicity scales and the one obtained by C09 for R97 for the visible.

uncertainties at high metallicities. Considering the scale of C09c (see Table 6), we have only three GCs with $|\Delta[Fe/H]| > 1\sigma$, namely NGC 2808, NGC 6397 and NGC 6528. This last is the only one with $|\Delta[Fe/H]| > 2\sigma$, with a resulting [Fe/H] $= +0.04$ dex, compared with the adopted value of $-0.17$ dex. The equation for the scale of H10 (see Table 7) presents more discrepancies, since five clusters show $|\Delta[Fe/H]| > 1\sigma$, namely NGC 2808, NGC 3201 ($-1.42$ dex instead of $-1.59$ dex), NGC 6528 ($+0.04$ dex instead of $-0.11$ dex), NGC 6624 (again with $\Delta[Fe/H] > 2\sigma$), and NGC 6809 ($-1.81$ dex instead of $-1.94$ dex). The equations from the R97 dataset presented more discrepancies in the derived metallicities for the calibrators of C09 than the data of S12, maybe because of the method used to determine the EWs, or the larger uncertainties in the measured EWs.

### 3.3. Metallicity distributions

We used the cubic calibration relations for the dataset of S12 and the quadratic ones for the dataset of R97 to calculate the metallicity for each star and obtain the metallicity distribution in each GC. The results for the clusters discussed in this section are shown in Figs. 13–29, while similar histograms for all the clusters in our sample are shown in Figs. 30–42; Figs. 15–42. The convolved frequency is drawn with a solid line, while the classical frequency is plotted with a dotted histogram. We chose a
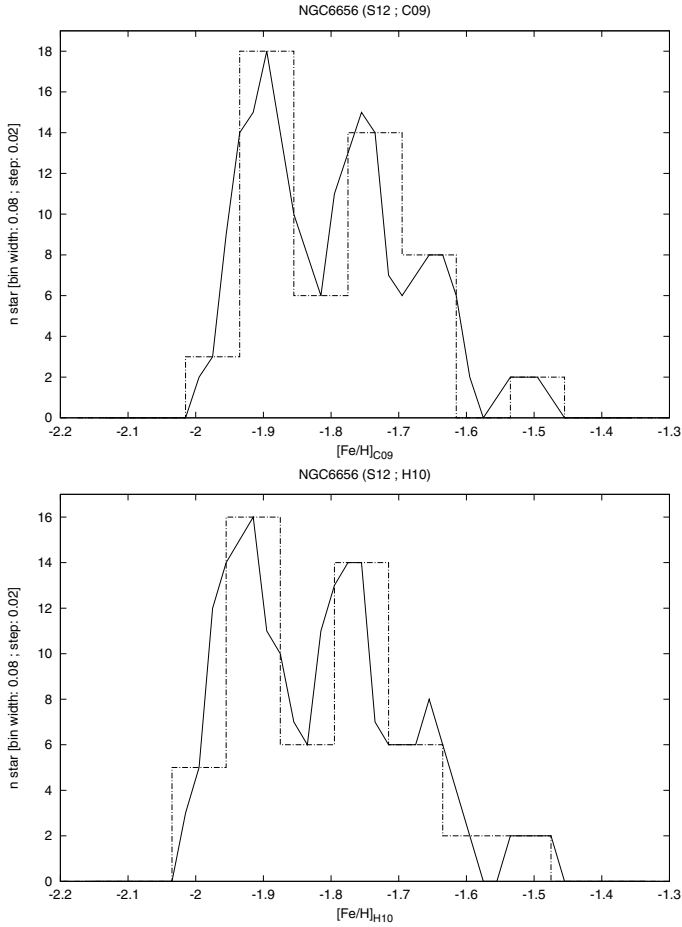
**Fig. 13.** Distribution in metallicity on the scale of C09 (*upper plot*) and H10 (*lower plot*) for NGC 6656 stars in the sample of S12.



**Fig. 14.** Distribution in metallicity for NGC 6656 stars from optical rEW.

bin width of 0.08 dex. The convolved frequency was obtained by shifting the position of the bin by a step of 0.02 dex, a quarter of the bin width, instead of using bins placed side by side. The analysis of the convolved frequency permits one to remove the bias introduced by the choice of the minimum value. We show the distribution of C09 for the GCs included in the two spectroscopic datasets, and both the distributions of C09 and H10 for the GCs with only one spectroscopic dataset.

NGC 6656 (M 22) presents a clear multimodal distribution (see Fig. 13), similar to the one shown in Da Costa et al. (2009), based on the same spectroscopic data. In Fig. 14 we show the distributions of the metallicities obtained from the optical rEW, which are sampled in the same way as our distributions, for the values calculated in Da Costa et al. (2009, upper plot) and S12 (lower plot). Both studies analyzed 51 stars, but their data reduction differed. The metallicity bimodality stands out more clearly with our rEW than it did with the optical data from Da Costa et al. (2009) and S12. The metallicity distributions based on optical magnitudes have a FWHM of ≈0.4 dex, while it reduces to 0.3 dex when based on NIR photometry. In the latter case, the peaks are also 30–50% higher. This result can be explained by the smaller effect of differential reddening when $K_s$ data are used. The calibration is not the source of these differences, because the ([Fe/H]; $\langle W' \rangle$) relation for optical and NIR data are very similar and approximately linear in the metallicity range under study. The main peak (located at [Fe/H] $\simeq -1.90$ dex in all the distributions) and the overall distribution is quite
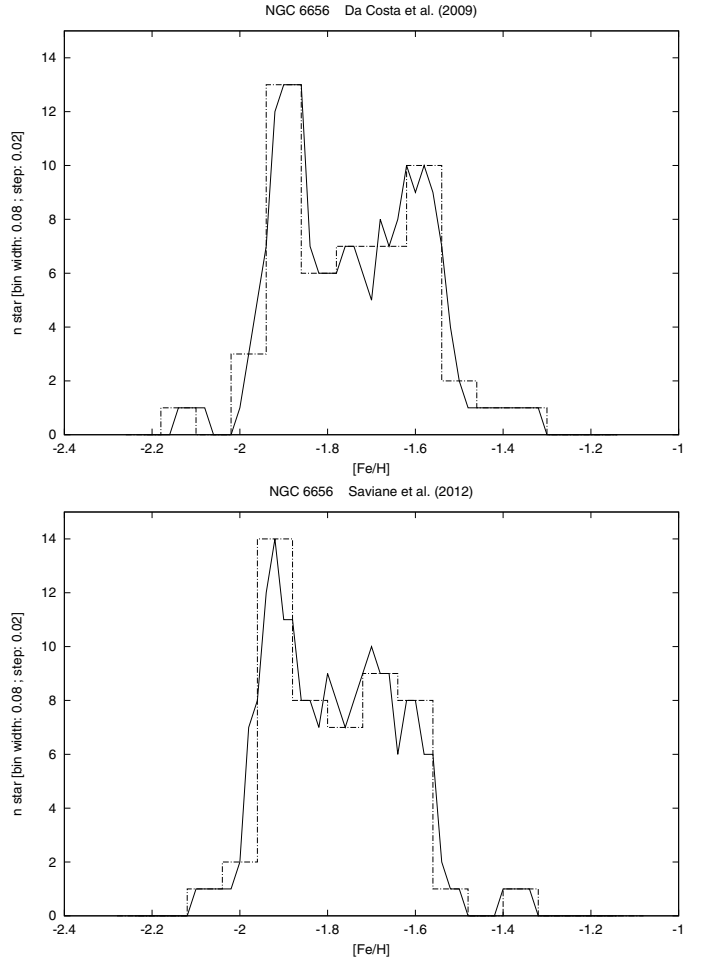
similar in the two plots based on optical photometry, although the secondary peak is more evident in the data of Da Costa (with a mean [Fe/H] value of ∼−1.60) than in the data of S12, where it is also located at ∼−1.70 dex. Hence, the differences in data reduction have not influenced the results noticeably. In our distribution, the two peaks are located at −1.77 and −1.90 dex, presenting a systematic shift of ≈0.08 dex with respect to the results found by Marino et al. (2009), who determined mean [Fe/H] values of −1.68 and −1.82 dex for stars rich and poor in s-process element, respectively.

NGC 6656 is not the only GC in our sample that shows a structured metallicity distribution suggesting a complex mix of stellar populations with different metallicity. The most peculiar distributions are those of NGC 6528 and NGC 6553, which are nearly flat and cover a ∼1 dex range in metallicity. Membership cannot be considered certain, since it is only based on position and radial velocity. They are also the two most metal-rich clusters, and the literature presents controversial values for their metallicity.

## 4. Discussion and conclusions

We determined $K_s$(HB) values for 30 GGCs. We then calculated the calibration equations between the metallicity and the rEW of the CaT using NIR photometry. We considered the GCs in the catalogs of equivalent widths presented in S12 and R97. We

presented the calibration equations on three metallicity scales: the scale presented in C09, the scale of C09 with recent high-resolution spectroscopic metallicities (C09c, see Sect. 2.3), and the values listed in H10. For the dataset of S12, the cubic relations (Eqs. (4), (6), and (8)) have the smallest urms, while for the dataset of R97 the quadratic relations (Eqs. (10), (12), and (14)) yield the best fits. The analysis of these solutions and of the metallicities obtained through them provide the following important points:

- The comparison between the calibration equations on the three metallicity scales demonstrates that, within ~0.05 dex, the three scales are equivalent. This similarity is not surprising since the other two scales are based on that of C09, even if they differ in individual values and in the determination. This result ensures the overall validity of the obtained equations, because the differences in the metallicities of some GCs slightly affect the fit. The validity of the solutions for the dataset of S12 is ensured by the small scatter shown by the calibrator GCs of C09, which can be assumed to have a well-determined metallicity (seven out eight of the calibrators included in the dataset of S12 present |Δ[Fe/H]| ≤ 0.05 dex).
- The calibration is independent of the passband used to calculate the rEW, as demonstrated by the comparison between the calibrations obtained from visible (~0.5 $\mu$m) and NIR (~2 $\mu$m) photometry. This result permits one to apply our relations even to $\langle W' \rangle$ calculated with magnitudes from other passbands.
- The comparison between the metallicity distributions for NGC 6656 (M 22) presented in Da Costa et al. (2009) and the one obtained from our calibrations (see Figs. 13 and 14) demonstrates that NIR CaT rEW are less affected by internal scatter (most likely produced by differential reddening in this cluster). The separation between the two main peaks in our distribution agrees with the metallicity difference between stars rich and poor in s-process element found by Marino et al. (2009), while the absolute positions are shifted by ~0.08 dex. The well-defined peaks demonstrate that the NIR CaT rEW is very promising as a powerful tool for studying metallicity distributions of GCs, especially clusters belonging to the Galactic bulge, where differential reddening is much stronger.
- The analysis of the metallicity distribution of our sample (Figs. 15–29) suggests peculiarities in some of the GCs. NGC 6528 and NGC 6553 (the two most metal-rich ones) show an almost flat distribution that covers approximately 0.5–1 dex. For NGC 6553, a similar spread of 0.5 dex was pointed out by Alves-Brito et al. (2006) for HR spectroscopic values present in the literature.
- NGC 3201 presents a spread in the metallicity distribution that suggests the presence of a complex metallicity population, as proposed by Simmerer et al. (2013), where the metallicity of 24 RGB stars were analyzed. This was also supported by Muñoz et al. (2013). Our distributions present a similar spread in [Fe/H] of 0.3 dex, but also a hint of a double peak. Seven of the 24 stars are in common with the 17 stars selected from the catalog of R97, while only one is present in the sample of S12. The stars in common with R97 present a metallicity difference smaller than ~0.1 dex with a mean value of +0.04 dex, and the same value for the difference with the metallicity reported in C09; five stars present an absolute metallicity difference smaller than 0.05 dex with a mean difference of +0.02 dex, where Simmerer et al. (2013) declared a total uncertainty in [Fe/H] smaller than 0.15 dex.

This result confirms the accuracy of the [Fe/H] values obtained through the CaT method compared with those obtained with HR spectroscopy.
- We also detected possible complex distributions also for other GCs, namely NGC 2808, NGC 6121 (M 4), NGC 6356, NGC 6440, NGC 6522, NGC 6541, NGC 6569, NGC 6624, NGC 6626 (M 28), NGC 6637 (M 69), NGC 6638, and Pal 7 (IC 1276). NGC 6440 and NGC 6569 are also suggested to have a double horizontal branch in Mauro et al. (2012), while NGC 6626 is a metal-poor cluster that presents parameters very similar to NGC 6656, such as metallicity, absolute magnitude, and CMD shape. For these three GCs, HR spectra were obtained and are under study.

A comparison with previous results of metallicities obtained from the CaT method with NIR photometry did not lead to meaningful conclusions because Warren & Cole (2009) and Lane et al. (2010) calibrated on different scales (CG97 and Harris 1996, respectively) and, except for NGC 6656, all the other GCs in common are also calibrators of C09, whose metallicities agree well with our results.

## References

Alves-Brito, A., Barbuy, B., Zoccali, M., et al. 2006, A&A, 460, 269
Appenzeller, I., Fricke, K., Fürtig, W., et al. 1998, The Messenger, 94, 1
Armandroff, T. E., & Da Costa, G. S. 1991, AJ, 101, 1329
Barbuy, B., Zoccali, M., Ortolani, S., et al. 2007, AJ, 134, 1613
Battaglia, G., Irwin, M., Tolstoy, E., et al. 2008, MNRAS, 383, 183
Battaglia, G., Tolstoy, E., Helmi, A., et al. 2011, MNRAS, 411, 1013
Bressan, A., Marigo, P., Girardi, L., et al. 2012, MNRAS, 427, 127
Buzzoni, A., Pecci, F. F., Buonanno, R., & Corsi, C. E. 1983, A&A, 128, 94
Carrera, R., Pancino, E., Gallart, C., & del Pino, A. 2013, MNRAS, 434, 1681
Carretta, E., & Gratton, R. G. 1997, A&AS, 121, 95
Carretta, E., Cohen, J. G., Gratton, R. G., & Behr, B. B. 2001, AJ, 122, 1469
Carretta, E., Bragaglia, A., Gratton, R. G., et al. 2009, A&A, 505, 117
Cassisi, S., Salaris, M., & Irwin, A. W. 2003, ApJ, 588, 862
Catelan, M., Minniti, D., Lucas, P. W., et al. 2011, in RR Lyrae Stars, Metal-Poor Stars, and the Galaxy, ed. A. McWilliam, vol. 5 (Pasadena: the Observatories of the Carnegie Institution of Washington), 145
Cenarro, A. J., Cardiel, N., & Gorgas, J. 2008, in Pathways Through an Eclectic Universe, eds. J. H. Knapen, T. J. Mahoney, & A. Vazdekis, ASP Conf. Ser., 390, 292
Chené, A.-N., Borissova, J., Clarke, J. R. A., et al. 2012, A&A, 545, A54
Cole, A. A., Smecker-Hane, T. A., & Gallagher, III, J. S. 2000, AJ, 120, 1808
Cole, A. A., Smecker-Hane, T. A., Tolstoy, E., Bosler, T. L., & Gallagher, J. S. 2004, MNRAS, 347, 367
Da Costa, G. S., & Armandroff, T. E. 1995, AJ, 109, 2533
Da Costa, G. S., Held, E. V., Saviane, I., & Gullieuszik, M. 2009, ApJ, 705, 1481
Emerson, J., & Sutherland, W. 2010, The Messenger, 139, 2
Ferraro, F. R., Valenti, E., & Origlia, L. 2006, ApJ, 649, 243
Ferraro, F. R., Dalessandro, E., Mucciarelli, A., et al. 2009, Nature, 462, 483
Foster, C., Forbes, D. A., Proctor, R. N., et al. 2010, AJ, 139, 1566
Girardi, L., & Salaris, M. 2001, MNRAS, 323, 109
Gullieuszik, M., Held, E. V., Saviane, I., & Rizzi, L. 2009, A&A, 500, 735
Harris, W. E. 1996, AJ, 112, 1487
Harris, W. E. 2010, unpulished [arXiv:1012.3224]
Idiart, T. P., Thevenin, F., & de Freitas Pacheco, J. A. 1997, AJ, 113, 1066
Irwin, M. J., Lewis, J., Hodgkin, S., et al. 2004, in Proc. SPIE, 5493, eds. P. J. Quinn, & A. Bridger, 411

Izzo, C., de Bilbao, L., Larsen, J., et al. 2010, in Proc. SPIE, 7737, 29
Jones, J. E., Alloin, D. M., & Jones, B. J. T. 1984, ApJ, 283, 457
Lane, R. R., Kiss, L. L., Lewis, G. F., et al. 2010, MNRAS, 401, 2521
Marino, A. F., Milone, A. P., Piotto, G., et al. 2009, A&A, 505, 1099
Mauro, F., Moni Bidin, C., Cohen, R., et al. 2012, ApJ, 761, L29
Mauro, F., Moni Bidin, C., Chené, A.-N., et al. 2013, Rev. Mex. Astron. Astrofís., 49, 189
McWilliam, A., & Rich, R. M. 1994, ApJS, 91, 749
Minniti, D. 1995, A&AS, 113, 299
Minniti, D., Lucas, P. W., Emerson, J. P., et al. 2010, New Astron., 15, 433
Momany, Y., Ortolani, S., Held, E. V., et al. 2003, A&A, 402, 607
Moni Bidin, C., Mauro, F., Geisler, D., et al. 2011, A&A, 535, A33
Muñoz, C., Geisler, D., & Villanova, S. 2013, MNRAS, 433, 2006
Nataf, D. M., Gould, A. P., Pinsonneault, M. H., & Udalski, A. 2013, ApJ, 766, 77
Olszewski, E. W., Schommer, R. A., Suntzeff, N. B., & Harris, H. C. 1991, AJ, 101, 515
Origlia, L., Valenti, E., & Rich, R. M. 2005, MNRAS, 356, 1276
Parisi, M. C., Geisler, D., Grocholski, A. J., Clariá, J. J., & Sarajedini, A. 2010, AJ, 139, 1168
Renzini, A. 1994, A&A, 285, L5

Rutledge, G. A., Hesser, J. E., & Stetson, P. B. 1997, PASP, 109, 907
Saito, R., Hempel, M., Alonso-García, J., et al. 2010, The Messenger, 141, 24
Saito, R. K., Hempel, M., Minniti, D., et al. 2012, A&A, 537, A107
Salaris, M., & Girardi, L. 2002, MNRAS, 337, 332
Saviane, I., da Costa, G. S., Held, E. V., et al. 2012, A&A, 540, A27
Simmerer, J., Ivans, I. I., Filler, D., et al. 2013, ApJ, 764, L7
Skrutskie, M. F., Cutri, R. M., Stiening, R., et al. 2006, AJ, 131, 1163
Sobeck, J. S., Ivans, I. I., Simmerer, J. A., et al. 2006, AJ, 131, 2949
Stetson, P. B. 1987, PASP, 99, 191
Stetson, P. B. 1994, PASP, 106, 250
Valenti, E., Origlia, L., & Ferraro, F. R. 2005, MNRAS, 361, 272
Valenti, E., Ferraro, F. R., & Origlia, L. 2007, AJ, 133, 1287
Valenti, E., Ferraro, F. R., & Origlia, L. 2010, MNRAS, 402, 1729
Valenti, E., Origlia, L., & Rich, R. M. 2011, MNRAS, 414, 2690
Warren, S. R., & Cole, A. A. 2009, MNRAS, 393, 272
Zinn, R. 1985, ApJ, 293, 424
Zinn, R., & West, M. J. 1984, ApJS, 55, 45
Zoccali, M., Cassisi, S., Bono, G., et al. 2000, ApJ, 538, 289
Zoccali, M., Barbuy, B., Hill, V., et al. 2004, A&A, 423, 507

**Table 2.** Metallicities for the GCs of S12 in the scale of C09.

| GC (1) | [Fe/H] (2) | ⟨W'⟩ (3) | [Fe/H]$_1$ (Ia) | Δ (Ib) | Δ/σ (Ic) | [Fe/H]$_2$ (IIa) | Δ (IIb) | Δ/σ (IIc) | [Fe/H]$_3$ (IIIa) | Δ (IIIb) | Δ/σ (IIIc) | [Fe/H]$_4$ (IVa) | Δ (IVb) | Δ/σ (IVc) | [Fe/H]$_5$ (Va) | Δ (Vb) | Δ/σ (Vc) |
|---|---|---|---|---|---|---|---|---|---|---|---|---|---|---|---|---|---|
| NGC 2808 | −1.18 | 4.47 | −1.12 | −0.06 | −0.2 | −1.14 | −0.04 | −0.2 | −1.19 | +0.01 | +0.0 | −1.19 | +0.01 | +0.0 | −1.18 | −0.00 | −0.0 |
| NGC 3201 | −1.51 | 3.91 | −1.40 | −0.11 | −0.4 | −1.47 | −0.04 | −0.2 | −1.47 | −0.04 | −0.2 | −1.47 | −0.04 | −0.2 | −1.47 | −0.04 | −0.1 |
| NGC 6121 | −1.18 | 4.40 | −1.16 | −0.02 | −0.1 | −1.19 | +0.01 | +0.0 | −1.23 | +0.05 | +0.2 | −1.23 | +0.05 | +0.2 | −1.22 | −0.04 | −0.2 |
| NGC 6139* | −1.71 | 3.92 | −1.40 | −0.31 | −1.1 | −1.47 | −0.24 | −1.1 | −1.47 | −0.24 | −1.1 | −1.47 | −0.24 | −1.1 | −1.47 | −0.24 | −1.0 |
| NGC 6254 | −1.57 | 3.70 | −1.51 | −0.06 | −0.2 | −1.59 | +0.02 | +0.1 | −1.57 | −0.00 | −0.0 | −1.57 | −0.00 | −0.0 | −1.58 | +0.01 | +0.0 |
| NGC 6325 | −1.37 | 4.36 | −1.17 | −0.20 | −0.7 | −1.21 | −0.16 | −0.7 | −1.25 | −0.12 | −0.6 | −1.25 | −0.12 | −0.5 | −1.24 | −0.13 | −0.5 |
| NGC 6356 | −0.35 | 5.28 | −0.70 | +0.35 | +1.2 | −0.60 | +0.25 | +1.1 | −0.58 | +0.23 | +1.1 | −0.58 | +0.23 | +1.0 | −0.59 | +0.24 | +1.0 |
| NGC 6380* | −0.40 | 5.11 | −0.79 | +0.39 | +1.3 | −0.72 | +0.32 | +1.4 | −0.73 | +0.33 | +1.5 | −0.73 | +0.33 | +1.5 | −0.74 | +0.34 | +1.4 |
| NGC 6397 | −1.99 | 2.66 | −2.04 | +0.05 | +0.2 | −2.06 | +0.07 | +0.3 | −1.99 | −0.00 | −0.0 | −1.99 | −0.00 | −0.0 | −1.98 | −0.01 | −0.0 |
| NGC 6440 | −0.20 | 5.48 | −0.60 | +0.40 | +1.4 | −0.45 | +0.25 | +1.1 | −0.38 | +0.18 | +0.8 | −0.38 | +0.18 | +0.8 | −0.39 | +0.19 | +0.8 |
| NGC 6441 | −0.44 | 5.20 | −0.74 | +0.30 | +1.0 | −0.65 | +0.21 | +0.9 | −0.65 | +0.21 | +1.0 | −0.65 | +0.21 | +0.9 | −0.66 | +0.22 | +0.9 |
| NGC 6528 | +0.07 | 5.65 | −0.51 | +0.58 | +2.0 | −0.32 | +0.39 | +1.7 | −0.19 | +0.26 | +1.2 | −0.19 | +0.26 | +1.1 | −0.19 | +0.26 | +1.1 |
| NGC 6553 | −0.16 | 5.76 | −0.46 | +0.30 | +1.0 | −0.23 | +0.07 | +0.3 | −0.06 | −0.10 | −0.5 | −0.06 | −0.10 | −0.5 | −0.04 | −0.12 | −0.5 |
| NGC 6558 | −1.37 | 4.62 | −1.04 | −0.33 | −1.1 | −1.05 | −0.32 | −1.4 | −1.09 | −0.28 | −1.3 | −1.09 | −0.28 | −1.2 | −1.08 | −0.29 | −1.2 |
| NGC 6569 | −0.72 | 4.44 | −1.13 | +0.41 | +1.4 | −1.16 | +0.44 | +1.9 | −1.20 | +0.48 | +2.3 | −1.20 | +0.48 | +2.2 | −1.19 | +0.47 | +2.0 |
| NGC 6656 | −1.70 | 3.07 | −1.83 | +0.13 | +0.5 | −1.89 | +0.19 | +0.8 | −1.82 | +0.12 | +0.6 | −1.82 | +0.12 | +0.5 | −1.83 | +0.13 | +0.5 |
| NGC 6838 | −0.82 | 5.07 | −0.81 | −0.01 | −0.0 | −0.75 | −0.07 | −0.3 | −0.77 | −0.05 | −0.2 | −0.77 | −0.05 | −0.2 | −0.77 | −0.05 | −0.2 |
| NGC 7078 | −2.33 | 2.01 | −2.38 | +0.05 | +0.2 | −2.28 | −0.05 | −0.2 | −2.33 | −0.00 | −0.0 | −2.33 | −0.00 | −0.0 | −2.33 | +0.00 | +0.0 |
| Pal 7 * | −0.65 | 5.22 | −0.73 | +0.08 | +0.3 | −0.64 | −0.01 | −0.1 | −0.63 | −0.02 | −0.0 | −0.63 | −0.02 | −0.1 | −0.64 | −0.01 | −0.0 |

**Notes.** Column (1) lists the cluster ID (the GCs marked with * were not used to calculate the calibration). Column (2) is the metallicity according to the scale. Column (3) is the calculated rEW. Column (Xa) is the metallicity based on the calibration using a polynomial of degree X. Column (Xb) is the difference between the calculated and the scale metallicity. Column (Xc) is the former difference in rms.

**Table 3.** Metallicities for the GCs of S12 in the scale of C09c.

| GC (1) | [Fe/H] (2) | ⟨W'⟩ (3) | [Fe/H]$_2$ (IIa) | Δ (IIb) | Δ/σ (IIc) | [Fe/H]$_3$ (IIIa) | Δ (IIIb) | Δ/σ (IIIc) | [Fe/H]$_4$ (IVa) | Δ (IVb) | Δ/σ (IVc) | [Fe/H]$_5$ (Va) | Δ (Vb) | Δ/σ (Vc) |
|---|---|---|---|---|---|---|---|---|---|---|---|---|---|---|
| NGC 2808 | −1.18 | 4.47 | −1.13 | −0.05 | −0.3 | −1.16 | −0.02 | −0.1 | −1.16 | −0.02 | −0.1 | −1.13 | −0.05 | −0.2 |
| NGC 3201 | −1.51 | 3.91 | −1.45 | −0.06 | −0.3 | −1.46 | −0.05 | −0.3 | −1.46 | −0.05 | −0.3 | −1.46 | −0.05 | −0.2 |
| NGC 6121 | −1.18 | 4.40 | −1.18 | −0.00 | −0.0 | −1.21 | +0.03 | +0.1 | −1.21 | +0.03 | +0.1 | −1.18 | −0.00 | −0.0 |
| NGC 6139* | −1.71 | 3.92 | −1.45 | −0.26 | −1.4 | −1.45 | −0.26 | −1.5 | −1.46 | −0.25 | −1.4 | −1.59 | −0.25 | −1.2 |
| NGC 6254 | −1.57 | 3.70 | −1.57 | +0.00 | +0.0 | −1.56 | −0.01 | −0.1 | −1.56 | −0.01 | −0.0 | −1.59 | +0.02 | +0.1 |
| NGC 6325 | −1.37 | 4.36 | −1.20 | −0.17 | −0.9 | −1.23 | −0.14 | −0.8 | −1.23 | −0.14 | −0.8 | −1.20 | −0.17 | −0.9 |
| NGC 6356 | −0.35 | 5.28 | −0.60 | +0.25 | +1.4 | −0.59 | +0.24 | +1.4 | −0.59 | +0.24 | +1.3 | −0.62 | +0.27 | +1.4 |
| NGC 6380* | −0.40 | 5.11 | −0.72 | +0.32 | +1.8 | −0.72 | +0.32 | +1.9 | −0.72 | +0.32 | +1.8 | −0.74 | +0.34 | +1.7 |
| NGC 6397 | −1.99 | 2.66 | −2.05 | +0.06 | +0.3 | −2.00 | +0.01 | +0.1 | −2.00 | +0.01 | +0.0 | −1.98 | −0.01 | −0.0 |
| NGC 6440 | −0.20 | 5.48 | −0.46 | +0.26 | +1.4 | −0.41 | +0.21 | +1.2 | −0.41 | +0.21 | +1.2 | −0.45 | +0.25 | +1.2 |
| NGC 6441 | −0.44 | 5.20 | −0.65 | +0.21 | +1.2 | −0.65 | +0.21 | +1.2 | −0.65 | +0.21 | +1.1 | −0.68 | +0.24 | +1.2 |
| NGC 6528 | −0.17 | 5.65 | −0.33 | +0.16 | +0.9 | −0.24 | +0.07 | +0.4 | −0.25 | +0.08 | +0.5 | −0.25 | +0.08 | +0.4 |
| NGC 6553 | −0.16 | 5.76 | −0.25 | +0.09 | +0.5 | −0.13 | −0.03 | −0.2 | −0.15 | −0.01 | −0.0 | −0.11 | −0.05 | −0.3 |
| NGC 6558 | −0.97 | 4.62 | −1.04 | +0.07 | +0.4 | −1.07 | +0.10 | +0.6 | −1.06 | +0.09 | +0.5 | −1.04 | +0.07 | +0.4 |
| NGC 6569 | −0.79 | 4.44 | −1.15 | +0.36 | +2.0 | −1.18 | +0.39 | +2.2 | −1.18 | +0.39 | +2.2 | −1.15 | +0.36 | +1.8 |
| NGC 6656 | −1.70 | 3.07 | −1.87 | +0.17 | +1.0 | −1.83 | +0.13 | +0.7 | −1.82 | +0.12 | +0.7 | −1.86 | +0.16 | +0.8 |
| NGC 6838 | −0.82 | 5.07 | −0.75 | −0.07 | −0.4 | −0.76 | −0.06 | −0.3 | −0.75 | −0.07 | −0.4 | −0.77 | −0.05 | −0.2 |
| NGC 7078 | −2.33 | 2.01 | −2.29 | −0.04 | −0.2 | −2.32 | −0.01 | −0.0 | −2.33 | −0.00 | −0.0 | −2.33 | +0.00 | +0.0 |
| Pal 7 * | −0.65 | 5.22 | −0.64 | −0.01 | −0.0 | −0.64 | −0.01 | −0.1 | −0.63 | −0.02 | −0.1 | −0.66 | +0.01 | +0.1 |

**Notes.** Column (1) lists the cluster ID (the GCs marked with * were not used to calculate the calibration). Column (2) is the metallicity according to the scale. Column (3) is the calculated rEW. Column (Xa) is the metallicity based on the calibration using a polynomial of degree X. Column (Xb) is the difference between the calculated and the scale metallicity. Column (Xc) is the former difference in rms.

**Table 4.** Metallicities for the GCs of S12 in the scale of H10.

| GC (1) | [Fe/H] (2) | ⟨W'⟩ (3) | [Fe/H]$_1$ (Ia) | Δ (Ib) | Δ/σ (Ic) | [Fe/H]$_2$ (IIa) | Δ (IIb) | Δ/σ (IIc) | [Fe/H]$_3$ (IIIa) | Δ (IIIb) | Δ/σ (IIIc) | [Fe/H]$_4$ (IVa) | Δ (IVb) | Δ/σ (IVc) | [Fe/H]$_5$ (Va) | Δ (Vb) | Δ/σ (Vc) |
|---|---|---|---|---|---|---|---|---|---|---|---|---|---|---|---|---|---|
| NGC 2808 | −1.14 | 4.47 | −1.05 | −0.09 | −0.5 | −1.13 | −0.01 | −0.1 | −1.15 | +0.01 | +0.1 | −1.17 | +0.03 | +0.1 | −1.16 | +0.02 | +0.1 |
| NGC 3201 | −1.59 | 3.91 | −1.38 | −0.21 | −1.1 | −1.48 | −0.11 | −0.7 | −1.46 | −0.13 | −0.8 | −1.49 | −0.10 | −0.6 | −1.49 | −0.10 | −0.6 |
| NGC 6121 | −1.16 | 4.40 | −1.10 | −0.06 | −0.3 | −1.18 | +0.02 | +0.1 | −1.20 | +0.04 | +0.2 | −1.22 | +0.06 | +0.3 | −1.21 | +0.05 | +0.3 |
| NGC 6139 | −1.65 | 3.92 | −1.38 | −0.27 | −1.4 | −1.48 | −0.17 | −1.1 | −1.46 | −0.19 | −1.2 | −1.48 | −0.17 | −1.0 | −1.49 | −0.16 | −0.9 |
| NGC 6254 | −1.56 | 3.70 | −1.51 | −0.05 | −0.3 | −1.60 | +0.04 | +0.2 | −1.56 | +0.00 | +0.0 | −1.58 | +0.02 | +0.1 | −1.59 | +0.03 | +0.2 |
| NGC 6325 | −1.25 | 4.36 | −1.12 | −0.13 | −0.7 | −1.21 | −0.04 | −0.3 | −1.22 | −0.03 | −0.2 | −1.24 | −0.01 | −0.1 | −1.24 | −0.01 | −0.1 |
| NGC 6356 | −0.40 | 5.28 | −0.57 | +0.17 | +0.9 | −0.54 | +0.14 | +0.8 | −0.55 | +0.15 | +0.9 | −0.53 | +0.13 | +0.8 | −0.53 | +0.13 | +0.7 |
| NGC 6380 | −0.75 | 5.11 | −0.67 | −0.08 | −0.4 | −0.67 | −0.08 | −0.5 | −0.69 | −0.06 | −0.3 | −0.67 | −0.08 | −0.5 | −0.67 | −0.08 | −0.5 |
| NGC 6397 | −2.02 | 2.66 | −2.13 | +0.11 | +0.6 | −2.07 | +0.05 | +0.3 | −2.02 | +0.00 | +0.0 | −1.96 | −0.06 | −0.3 | −1.96 | −0.06 | −0.3 |
| NGC 6440 | −0.36 | 5.48 | −0.45 | +0.09 | +0.5 | −0.37 | +0.01 | +0.1 | −0.36 | +0.00 | +0.0 | −0.35 | −0.01 | −0.0 | −0.36 | −0.00 | −0.0 |
| NGC 6441 | −0.46 | 5.20 | −0.61 | +0.15 | +0.8 | −0.60 | +0.14 | +0.8 | −0.62 | +0.16 | +1.0 | −0.59 | +0.13 | +0.8 | −0.59 | +0.13 | +0.8 |
| NGC 6528 | −0.11 | 5.65 | −0.35 | +0.24 | +1.3 | −0.22 | +0.11 | +0.7 | −0.18 | +0.07 | +0.5 | −0.20 | +0.09 | +0.6 | −0.20 | +0.09 | +0.5 |
| NGC 6553 | −0.18 | 5.76 | −0.28 | +0.10 | +0.5 | −0.13 | −0.05 | −0.3 | −0.07 | −0.11 | −0.7 | −0.11 | −0.07 | −0.4 | −0.11 | −0.07 | −0.4 |
| NGC 6558 | −1.32 | 4.62 | −0.96 | −0.36 | −1.9 | −1.03 | −0.29 | −1.8 | −1.06 | −0.26 | −1.6 | −1.06 | −0.26 | −1.6 | −1.06 | −0.26 | −1.5 |
| NGC 6569 | −0.76 | 4.44 | −1.07 | +0.31 | +1.6 | −1.15 | +0.39 | +2.4 | −1.17 | +0.41 | +2.5 | −1.18 | +0.42 | +2.5 | −1.18 | +0.42 | +2.4 |
| NGC 6656 | −1.70 | 3.07 | −1.88 | +0.18 | +1.0 | −1.90 | +0.20 | +1.2 | −1.84 | +0.14 | +0.9 | −1.81 | +0.11 | +0.7 | −1.81 | +0.11 | +0.6 |
| NGC 6838 | −0.78 | 5.07 | −0.70 | −0.08 | −0.4 | −0.70 | −0.08 | −0.5 | −0.73 | −0.05 | −0.3 | −0.71 | −0.07 | −0.4 | −0.71 | −0.07 | −0.4 |
| NGC 7078 | −2.37 | 2.01 | −2.52 | +0.15 | +0.8 | −2.27 | −0.10 | −0.6 | −2.34 | −0.03 | −0.2 | −2.38 | +0.01 | +0.0 | −2.38 | +0.01 | +0.0 |
| Pal7 | −0.75 | 5.22 | −0.60 | −0.15 | −0.8 | −0.58 | −0.17 | −1.0 | −0.60 | −0.15 | −0.9 | −0.58 | −0.17 | −1.0 | −0.58 | −0.17 | −1.0 |

**Notes.** Column (1) lists the cluster ID. Column (2) is the metallicity according to the scale. Column (3) is the calculated rEW. Column (Xa) is the metallicity based on the calibration using a polynomial of degree X. Column (Xb) is the difference between calculated and the scale metallicity. Column (Xc) is the former difference in rms.

**Table 5.** Metallicities for the GCs of R97 in the scale of C09.

| GC (1) | [Fe/H] (2) | ⟨W'⟩ (3) | [Fe/H]$_1$ (Ia) | Δ (Ib) | Δ/σ (Ic) | [Fe/H]$_2$ (IIa) | Δ (IIb) | Δ/σ (IIc) | [Fe/H]$_3$ (IIIa) | Δ (IIIb) | Δ/σ (IIIc) |
|---|---|---|---|---|---|---|---|---|---|---|---|
| NGC 2808 | −1.18 | 3.80 | −1.26 | +0.08 | +0.4 | −1.31 | +0.13 | +1.3 | −1.32 | +0.14 | +1.3 |
| NGC 3201 | −1.51 | 3.59 | −1.39 | −0.12 | −0.6 | −1.47 | −0.04 | −0.4 | −1.47 | −0.04 | −0.3 |
| NGC 4372 | −2.19 | 2.07 | −2.25 | +0.06 | +0.3 | −2.21 | +0.02 | +0.2 | −2.20 | +0.01 | +0.1 |
| NGC 4590 | −2.27 | 1.98 | −2.30 | +0.03 | +0.1 | −2.23 | −0.04 | −0.4 | −2.23 | −0.04 | −0.3 |
| NGC 6121 | −1.18 | 3.98 | −1.16 | −0.02 | −0.1 | −1.18 | −0.00 | −0.0 | −1.19 | +0.01 | +0.1 |
| NGC 6397 | −1.99 | 2.29 | −2.13 | +0.14 | +0.6 | −2.14 | +0.15 | +1.4 | −2.12 | +0.13 | +1.2 |
| NGC 6522 | −1.45 | 3.72 | −1.31 | −0.14 | −0.7 | −1.37 | −0.08 | −0.8 | −1.38 | −0.07 | −0.6 |
| NGC 6528 | +0.07 | 5.35 | −0.38 | +0.45 | +2.1 | +0.15 | −0.08 | −0.8 | +0.22 | −0.15 | −1.3 |
| NGC 6541 | −1.82 | 2.98 | −1.73 | −0.09 | −0.4 | −1.84 | +0.02 | +0.2 | −1.82 | +0.00 | +0.0 |
| NGC 6544 | −1.47 | 3.54 | −1.41 | −0.06 | −0.3 | −1.50 | +0.03 | +0.3 | −1.50 | +0.03 | +0.3 |
| NGC 6553 | −0.16 | 5.06 | −0.54 | +0.38 | +1.8 | −0.17 | +0.01 | +0.1 | −0.14 | −0.02 | −0.2 |
| NGC 6624 | −0.42 | 4.56 | −0.83 | +0.41 | +1.9 | −0.67 | +0.25 | +2.5 | −0.69 | +0.27 | +2.3 |
| NGC 6626* | −1.46 | 3.81 | −1.26 | −0.20 | −0.9 | −1.31 | −0.15 | −1.5 | −1.32 | −0.14 | −1.3 |
| NGC 6637 | −0.59 | 4.64 | −0.79 | +0.20 | +0.9 | −0.60 | +0.01 | +0.1 | −0.61 | +0.02 | +0.2 |
| NGC 6638 | −0.99 | 4.29 | −0.98 | −0.01 | −0.0 | −0.92 | −0.07 | −0.7 | −0.94 | −0.05 | −0.5 |
| NGC 6809 | −1.93 | 2.93 | −1.76 | −0.17 | −0.8 | −1.86 | −0.07 | −0.7 | −1.84 | −0.09 | −0.8 |
| NGC 7099 | −2.33 | 1.86 | −2.37 | +0.04 | +0.2 | −2.26 | −0.07 | −0.7 | −2.28 | −0.05 | −0.5 |

**Notes.** Column (1) lists the cluster ID (the GCs marked with * were not used to calculate the calibration). Column (2) is the metallicity according to the scale. Column (3) is the calculated rEW. Column (Xa) is the metallicity based on the calibration using a polynomial of degree X. Column (Xb) is the difference between the calculated and the scale metallicity. Column (Xc) is the former difference in rms.

**Table 6.** Metallicities for the GCs of R97 in the scale of C09c.

| GC (1) | [Fe/H] (2) | ⟨W'⟩ (3) | [Fe/H]₁ (Ia) | Δ (Ib) | Δ/σ (Ic) | [Fe/H]₂ (IIa) | Δ (IIb) | Δ/σ (IIc) | [Fe/H]₃ (IIIa) | Δ (IIIb) | Δ/σ (IIIc) |
|---|---|---|---|---|---|---|---|---|---|---|---|
| NGC 2808 | −1.18 | 3.80 | −1.27 | +0.09 | +0.5 | −1.32 | +0.14 | +1.5 | −1.32 | +0.14 | +1.4 |
| NGC 3201 | −1.51 | 3.59 | −1.39 | −0.12 | −0.7 | −1.47 | −0.04 | −0.5 | −1.47 | −0.04 | −0.4 |
| NGC 4372 | −2.19 | 2.07 | −2.25 | +0.06 | +0.4 | −2.21 | +0.02 | +0.2 | −2.21 | +0.02 | +0.2 |
| NGC 4590 | −2.27 | 1.98 | −2.30 | +0.03 | +0.2 | −2.23 | −0.04 | −0.4 | −2.24 | −0.03 | −0.3 |
| NGC 6121 | −1.18 | 3.98 | −1.17 | −0.01 | −0.1 | −1.19 | +0.01 | +0.1 | −1.20 | +0.02 | +0.2 |
| NGC 6397 | −1.99 | 2.29 | −2.13 | +0.14 | +0.8 | −2.13 | +0.14 | +1.5 | −2.13 | +0.14 | +1.3 |
| NGC 6522 | −1.45 | 3.72 | −1.31 | −0.14 | −0.8 | −1.38 | −0.07 | −0.8 | −1.38 | −0.07 | −0.7 |
| NGC 6528 | −0.17 | 5.35 | −0.39 | +0.22 | +1.4 | +0.04 | −0.21 | −2.2 | +0.07 | −0.24 | −2.3 |
| NGC 6541 | −1.82 | 2.98 | −1.73 | −0.09 | −0.5 | −1.83 | +0.01 | +0.1 | −1.82 | −0.00 | −0.0 |
| NGC 6544 | −1.47 | 3.54 | −1.42 | −0.05 | −0.3 | −1.50 | +0.03 | +0.3 | −1.50 | +0.03 | +0.3 |
| NGC 6553 | −0.16 | 5.06 | −0.56 | +0.40 | +2.4 | −0.25 | +0.09 | +1.0 | −0.24 | +0.08 | +0.8 |
| NGC 6624 | −0.69 | 4.56 | −0.84 | +0.15 | +0.9 | −0.72 | +0.03 | +0.3 | −0.72 | +0.03 | +0.3 |
| NGC 6626* | −1.28 | 3.81 | −1.26 | −0.02 | −0.1 | −1.31 | +0.03 | +0.3 | −1.32 | +0.04 | +0.4 |
| NGC 6637 | −0.59 | 4.64 | −0.80 | +0.21 | +1.3 | −0.66 | +0.07 | +0.7 | −0.66 | +0.07 | +0.6 |
| NGC 6638 | −0.99 | 4.29 | −0.99 | +0.00 | +0.0 | −0.95 | −0.04 | −0.4 | −0.95 | −0.04 | −0.3 |
| NGC 6809 | −1.93 | 2.93 | −1.76 | −0.17 | −1.0 | −1.85 | −0.08 | −0.8 | −1.84 | −0.09 | −0.8 |
| NGC 7099 | −2.33 | 1.86 | −2.37 | +0.04 | +0.2 | −2.27 | −0.06 | −0.6 | −2.28 | −0.05 | −0.5 |

**Notes.** Column (1) lists the cluster ID (the GCs marked with * were not used to calculate calibration). Column (2) is the metallicity according to the scale. Column (3) is the calculated rEW. Column (Xa) is the metallicity based on the calibration using a polynomial of degree X. Column (Xb) is the difference between the calculated and the scale metallicity. Column (Xc) is the former difference in rms.

**Table 7.** Metallicities for the GCs of R97 in the scale of H10.

| GC (1) | [Fe/H] (2) | ⟨W'⟩ (3) | [Fe/H]₁ (Ia) | Δ (Ib) | Δ/σ (Ic) | [Fe/H]₂ (IIa) | Δ (IIb) | Δ/σ (IIc) | [Fe/H]₃ (IIIa) | Δ (IIIb) | Δ/σ (IIIc) |
|---|---|---|---|---|---|---|---|---|---|---|---|
| NGC 2808 | −1.14 | 3.80 | −1.18 | +0.04 | +0.2 | −1.27 | +0.13 | +1.2 | −1.26 | +0.12 | +1.2 |
| NGC 3201 | −1.59 | 3.59 | −1.32 | −0.27 | −1.8 | −1.42 | −0.17 | −1.5 | −1.43 | −0.16 | −1.5 |
| NGC 4372 | −2.17 | 2.07 | −2.28 | +0.11 | +0.7 | −2.19 | +0.02 | +0.2 | −2.19 | +0.02 | +0.2 |
| NGC 4590 | −2.23 | 1.98 | −2.34 | +0.11 | +0.7 | −2.23 | −0.00 | −0.0 | −2.20 | −0.03 | −0.3 |
| NGC 6121 | −1.16 | 3.98 | −1.07 | −0.09 | −0.6 | −1.15 | −0.01 | −0.1 | −1.12 | −0.04 | −0.4 |
| NGC 6397 | −2.02 | 2.29 | −2.14 | +0.12 | +0.8 | −2.11 | +0.09 | +0.8 | −2.15 | +0.13 | +1.3 |
| NGC 6522 | −1.34 | 3.72 | −1.23 | −0.11 | −0.7 | −1.33 | −0.01 | −0.1 | −1.33 | −0.01 | −0.1 |
| NGC 6528 | −0.11 | 5.35 | −0.19 | +0.08 | +0.5 | +0.04 | −0.15 | −1.3 | −0.04 | −0.07 | −0.7 |
| NGC 6541 | −1.81 | 2.98 | −1.70 | −0.11 | −0.7 | −1.78 | −0.03 | −0.2 | −1.85 | +0.04 | +0.4 |
| NGC 6544 | −1.40 | 3.54 | −1.34 | −0.06 | −0.4 | −1.45 | +0.05 | +0.5 | −1.47 | +0.07 | +0.6 |
| NGC 6553 | −0.18 | 5.06 | −0.38 | +0.20 | +1.3 | −0.24 | +0.06 | +0.6 | −0.24 | +0.06 | +0.6 |
| NGC 6624 | −0.44 | 4.56 | −0.70 | +0.26 | +1.7 | −0.69 | +0.25 | +2.3 | −0.64 | +0.20 | +1.9 |
| NGC 6626 | −1.32 | 3.81 | −1.17 | −0.15 | −1.0 | −1.27 | −0.05 | −0.5 | −1.26 | −0.06 | −0.6 |
| NGC 6637 | −0.64 | 4.64 | −0.65 | +0.01 | +0.1 | −0.63 | −0.01 | −0.1 | −0.58 | −0.06 | −0.6 |
| NGC 6638 | −0.95 | 4.29 | −0.87 | −0.08 | −0.5 | −0.91 | −0.04 | −0.4 | −0.86 | −0.09 | −0.9 |
| NGC 6809 | −1.94 | 2.93 | −1.73 | −0.21 | −1.3 | −1.81 | −0.13 | −1.2 | −1.88 | −0.06 | −0.6 |
| NGC 7099 | −2.27 | 1.86 | −2.42 | +0.15 | +1.0 | −2.27 | −0.00 | −0.0 | −2.21 | −0.06 | −0.6 |

**Notes.** Column (1) lists the cluster ID. Column (2) is the metallicity according to the scale. Column (3) is the calculated rEW. Column (Xa) is the metallicity based on the calibration using a polynomial of degree X. Column (Xb) is the difference between the calculated and the scale metallicity. Column (Xc) is the former difference in rms.
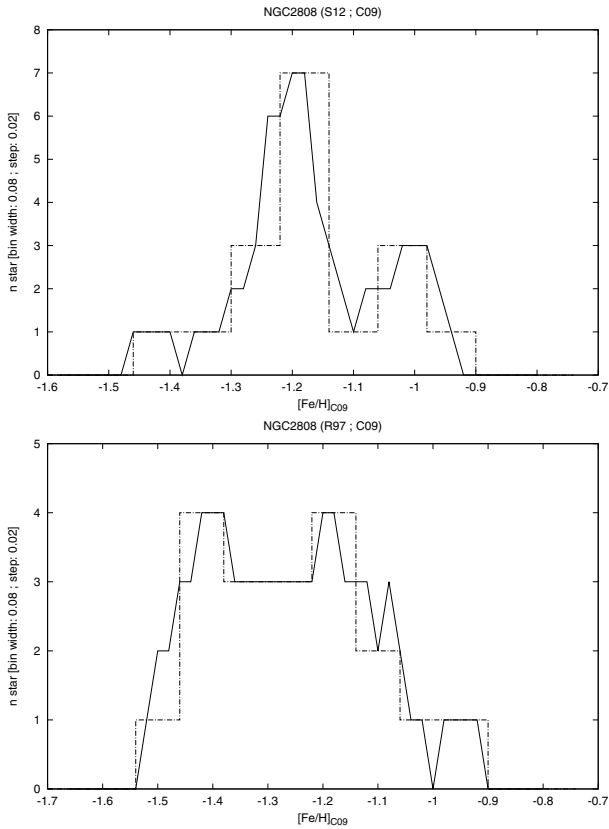
**Fig. 15.** Distribution in metallicity on the scale of C09 for NGC 2808 stars in the samples of S12 (*upper plot*) and R97 (*lower plot*).
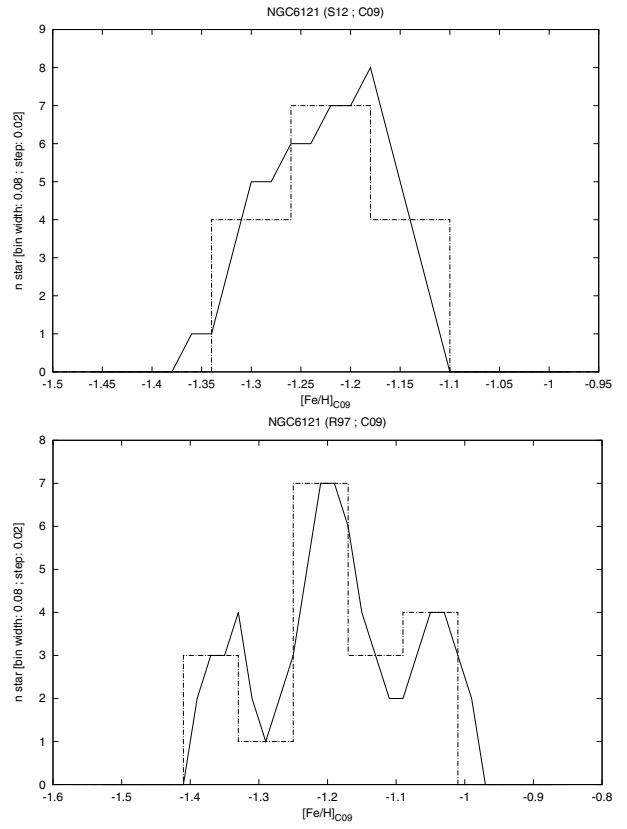


**Fig. 17.** Distribution in metallicity on the scale of C09 for NGC 6121 stars in the samples of S12 (*upper plot*) and R97 (*lower plot*).
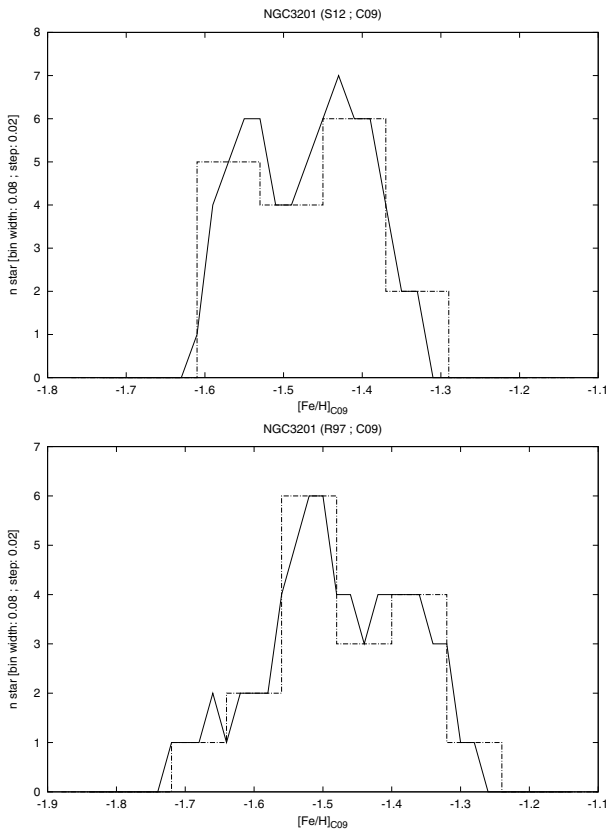


**Fig. 16.** Distribution in metallicity on the scale of C09 for NGC 3201 stars in the samples of S12 (*upper plot*) and R97 (*lower plot*).
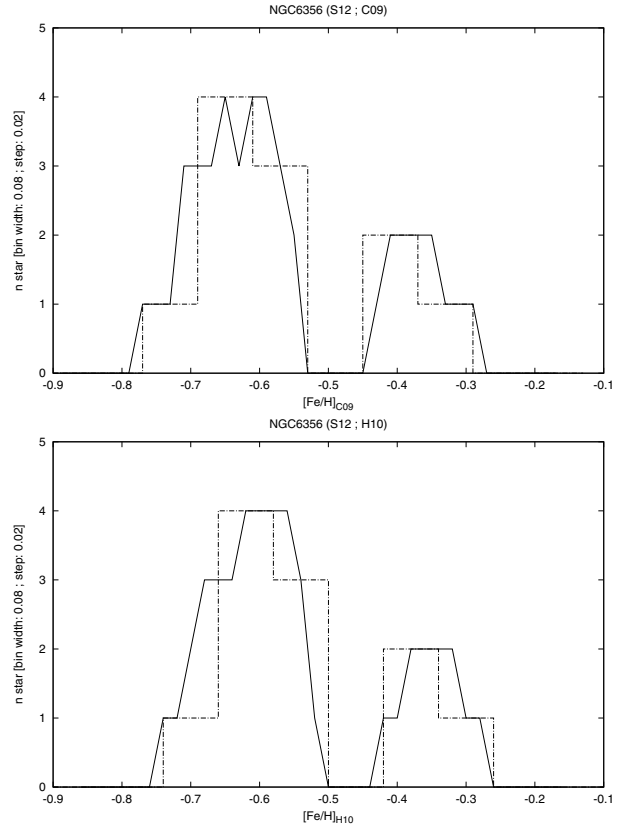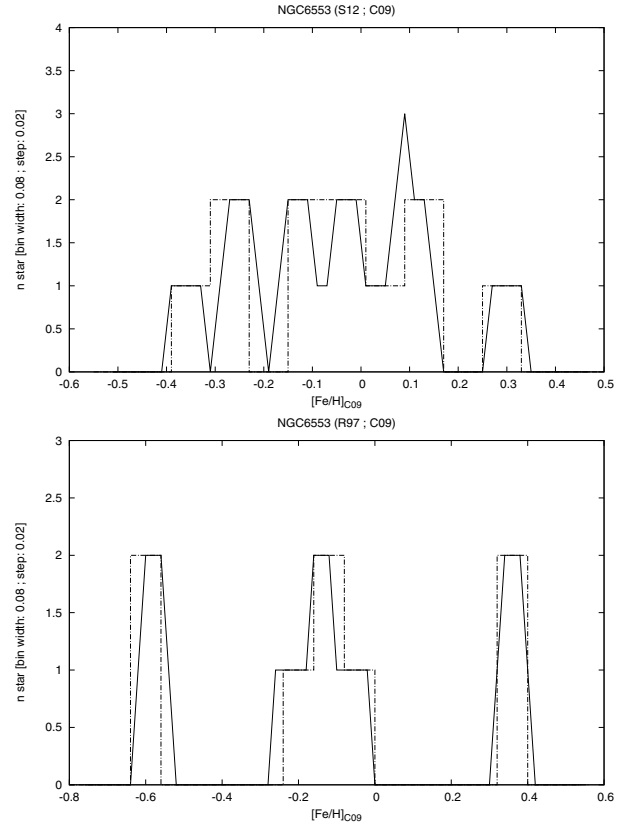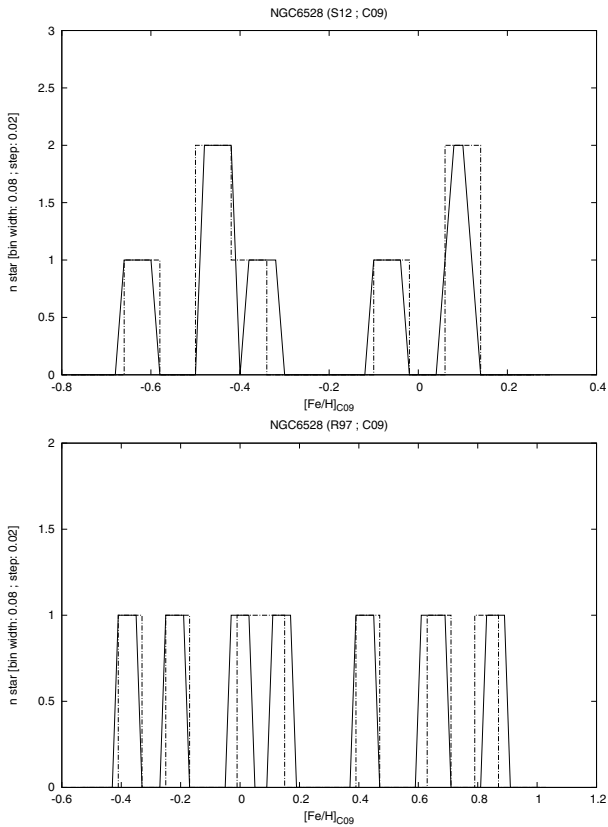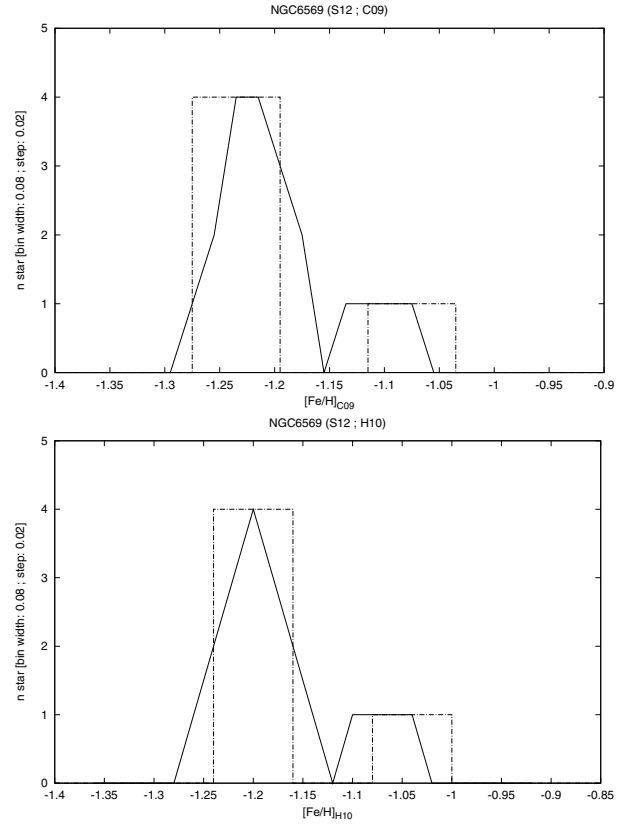


**Fig. 18.** Distribution in metallicity on the C09 (*upper plot*) and H10 (*lower plot*) scales for NGC 6356 stars in the sample of S12.
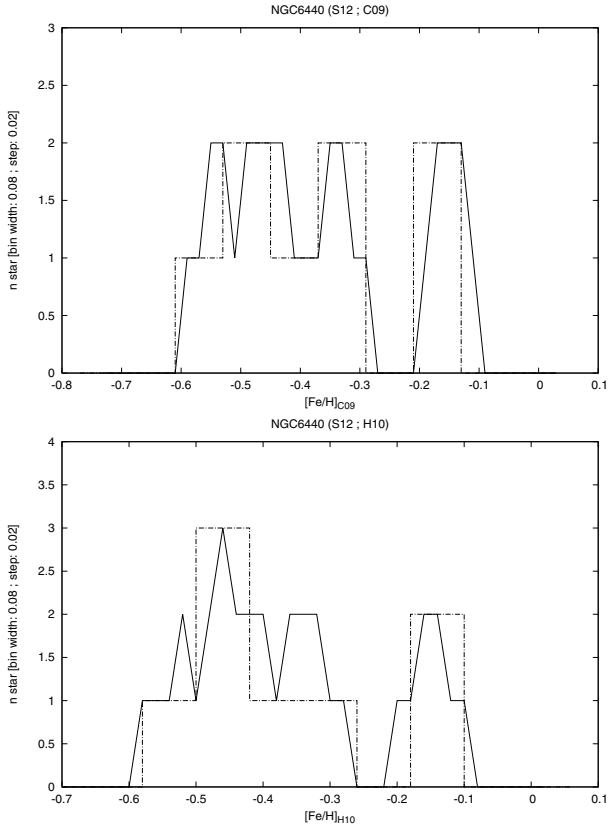
**Fig. 19.** Distribution in metallicity on the C09 (*upper plot*) and H10 (*lower plot*) scales for NGC 6440 stars in the sample of S12.



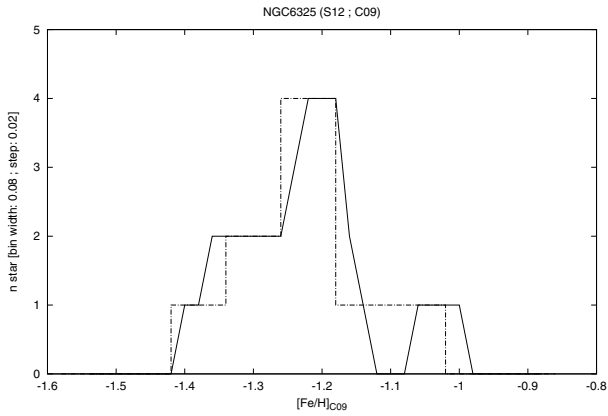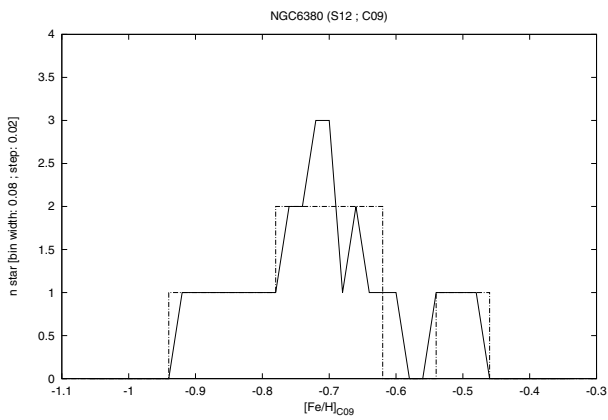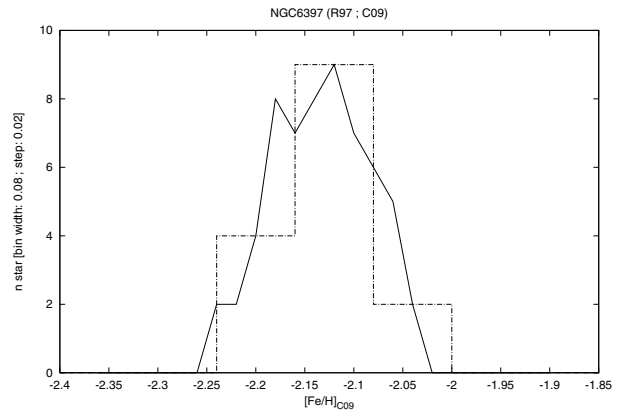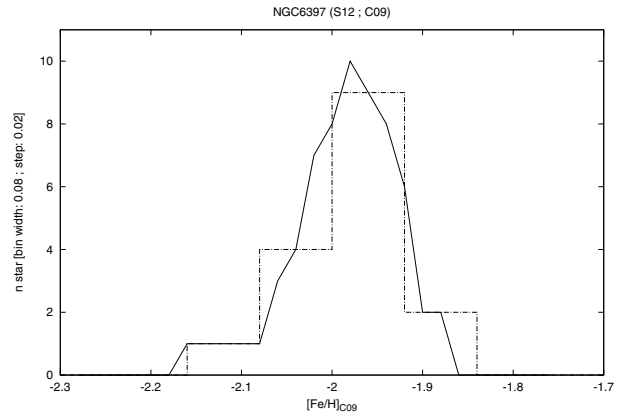**Fig. 21.** Distribution in metallicity on the scale of C09 for NGC 6553 stars in the samples of S12 (*upper plot*) and R97 (*lower plot*).



**Fig. 20.** Distribution in metallicity on the scale of C09 for NGC 6528 stars in the samples of S12 (*upper plot*) and R97 (*lower plot*).



**Fig. 22.** Distribution in metallicity on the C09 (*upper plot*) and H10 (*lower plot*) scales for NGC 6569 stars in the sample of S12.
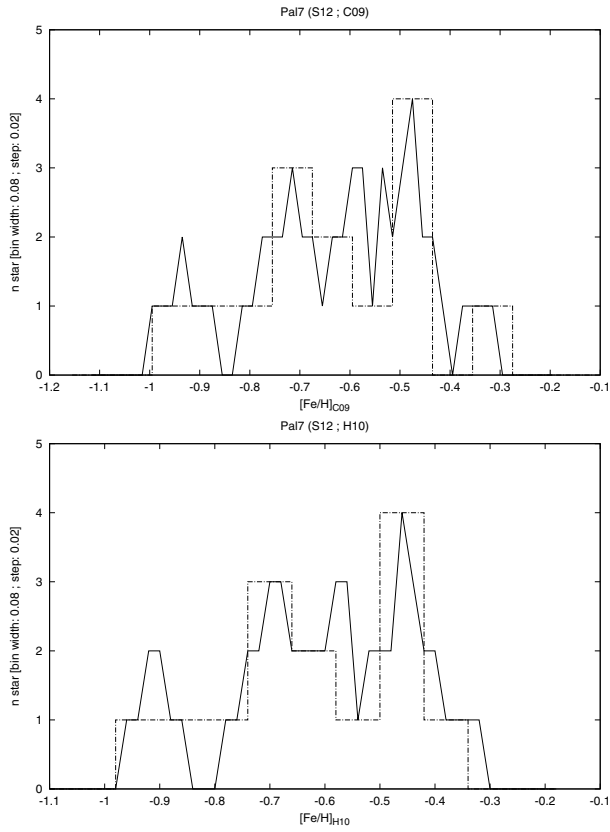
**Fig. 23.** Distribution in metallicity on the C09 (*upper plot*) and H10 (*lower plot*) scales for Pal 7 stars in the sample of S12.
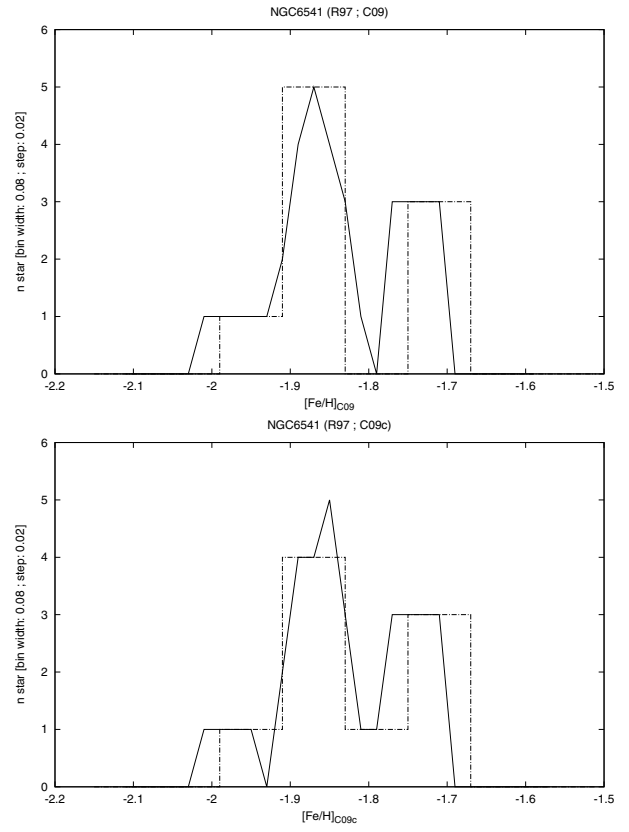
**Fig. 25.** Distribution in metallicity on the C09 (*upper plot*) and C09c (*lower plot*) scales for NGC 6541 stars in the sample of R97.
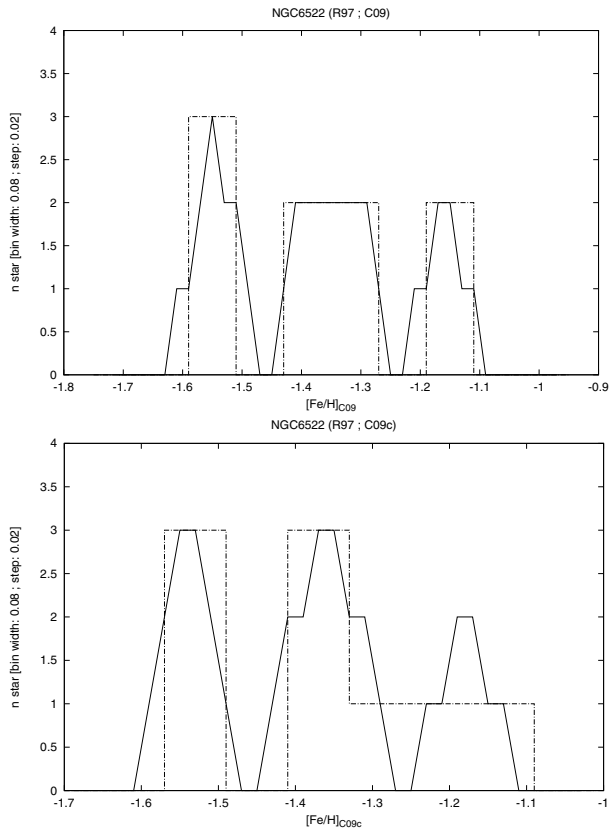
**Fig. 24.** Distribution in metallicity on the C09 (*upper plot*) and C09c (*lower plot*) scales for NGC 6522 stars in the sample of R97.
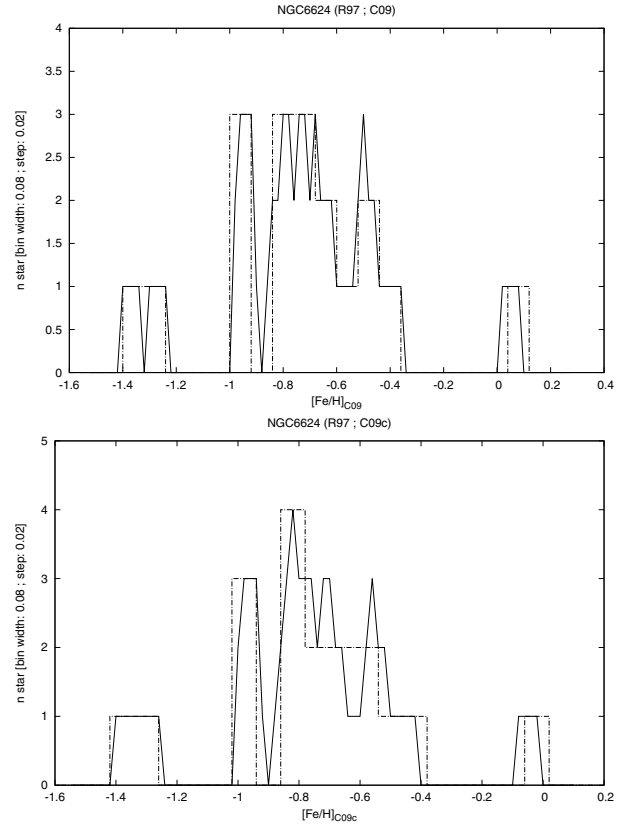
**Fig. 26.** Distribution in metallicity on the C09 (*upper plot*) and C09c (*lower plot*) scales for NGC 6624 stars in the sample of R97.
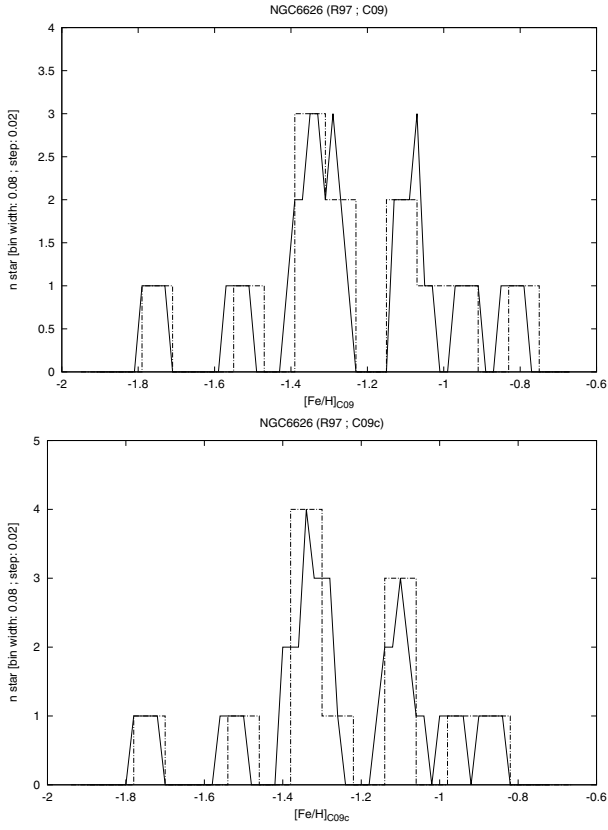
**Fig. 27.** Distribution in metallicity on the C09 (*upper plot*) and C09c (*lower plot*) scales for NGC 6626 stars in the sample of R97.
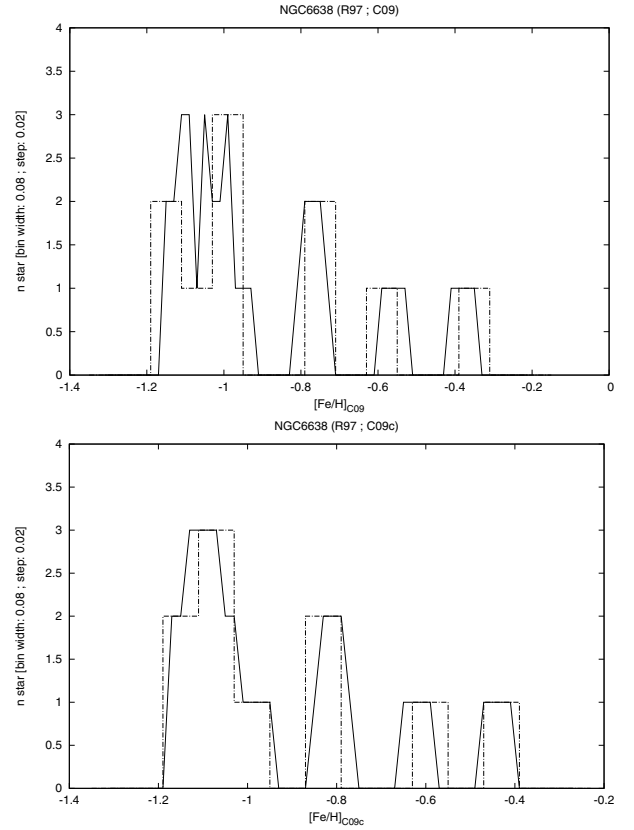


**Fig. 29.** Distribution in metallicity on the C09 (*upper plot*) and C09c (*lower plot*) scales for NGC 6638 stars in the sample of R97.
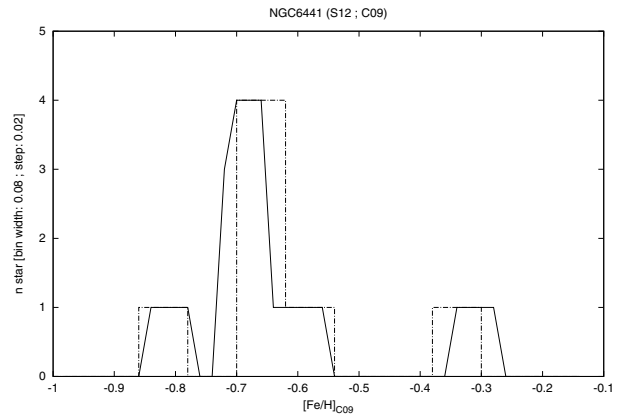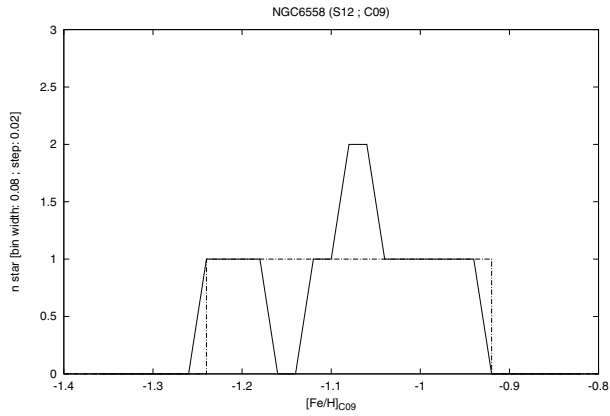


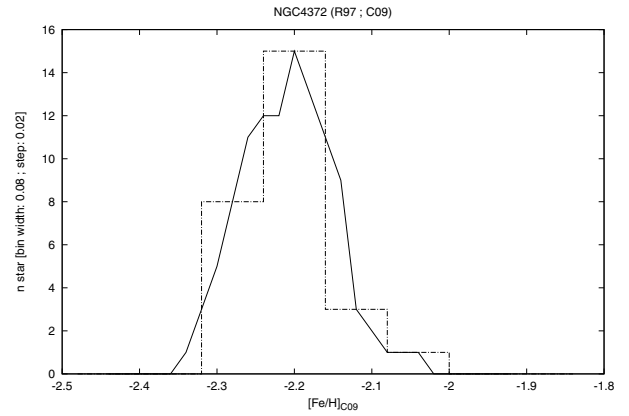**Fig. 30.** Distribution in metallicity on the scale of C09 for NGC 6254 stars in the sample of S12.



**Fig. 28.** Distribution in metallicity on the C09 (*upper plot*) and C09c (*lower plot*) scales for NGC 6637 stars in the sample of R97.

**Fig. 31.** Distribution in metallicity on the scale of C09 for NGC 6325 stars in the sample of S12.



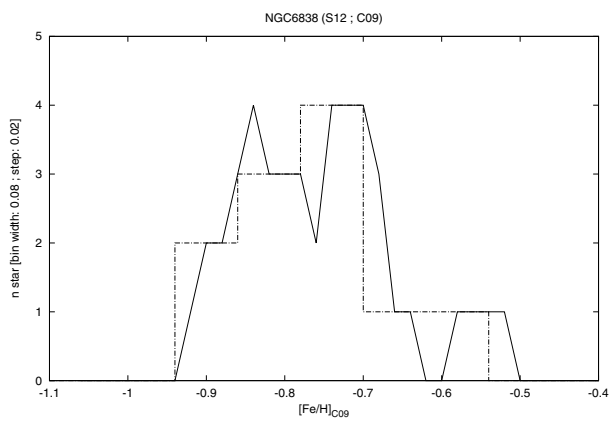**Fig. 32.** Distribution in metallicity on the scale of C09 for NGC 6380 stars in the sample of S12.





**Fig. 33.** Distribution in metallicity on the scale of C09 for NGC 6397 stars in the samples of S12 (*upper plot*) and R97 (*lower plot*).



**Fig. 34.** Distribution in metallicity on the scale of C09 for NGC 6441 stars in the sample of S12.

**Fig. 35.** Distribution in metallicity on the scale of C09 for NGC 6558 stars in the sample of S12.



**Fig. 38.** Distribution in metallicity on the scale of C09 for NGC 4372 stars in the sample of R97.



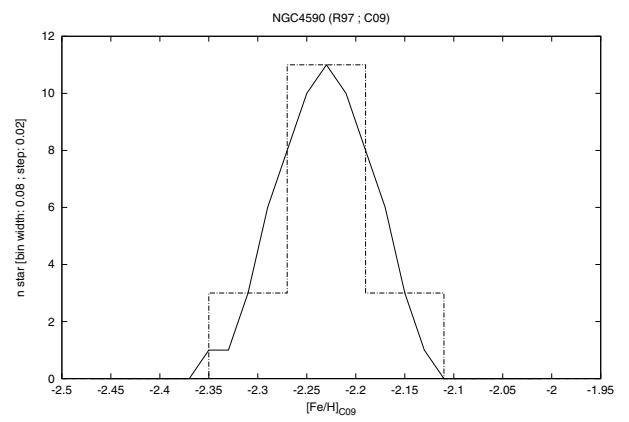**Fig. 36.** Distribution in metallicity on the scale of C09 for NGC 6838 stars in the sample of S12.



**Fig. 39.** Distribution in metallicity on the scale of C09 for NGC 4590 stars in the sample of R97.
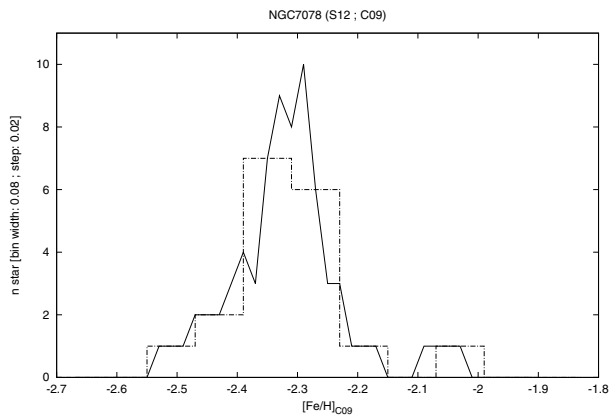


**Fig. 37.** Distribution in metallicity on the scale of C09 for NGC 7078 stars in the sample of S12.
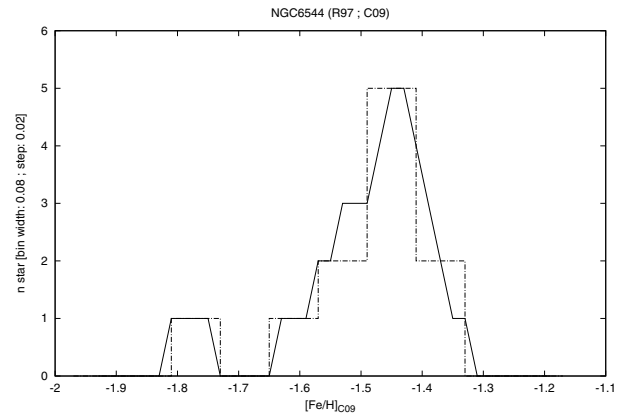


**Fig. 40.** Distribution in metallicity on the scale of C09 for NGC 6544 stars in the sample of R97.
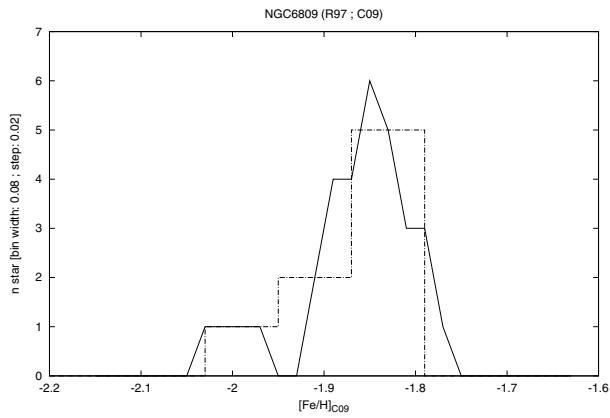
**Fig. 41.** Distribution in metallicity on the scale of C09 for NGC 6809 stars in the sample of R97.
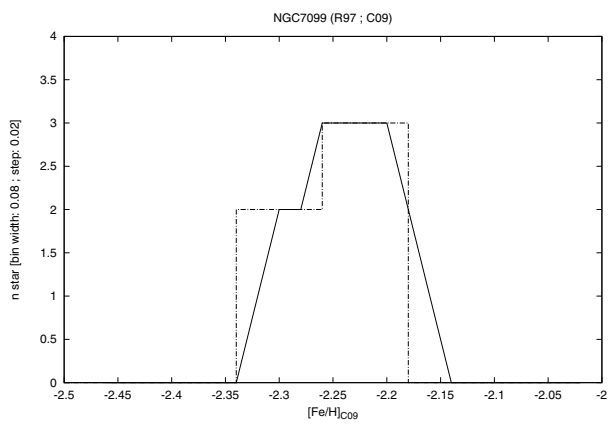


**Fig. 42.** Distribution in metallicity on the scale of C09 for NGC 7099 stars in the sample of R97.